

Computational Design of Crescent Shaped Promising Non-Fullerene Acceptors with 2,3-quinoxaline,1,4-dihydro Core and Different Electron-withdrawing Terminal Units for Photovoltaic Applications

Labanya Bhattacharya,¹Alex Brown², Sagar Sharma,³ and Sridhar Sahu^{1*}

¹*Computational Materials Research Lab, Department of Physics, Indian Institute of Technology (Indian School of Mines), Dhanbad, Jharkhand-826004, India*

²*Department of Chemistry, University of Alberta, Edmonton, Alberta, T6G 2G2, Canada*

³*Department of Chemistry, S. B. Deorah College, Bora Service, Ulubari, Guwahati-781007, Assam, India*

E-mail: *sridharsahu@iitism.ac.in

Abstract

This study aims to design a series of non-fullerene acceptors (NFAs) for photovoltaic applications having 2,3-quinoxalinedione,1,4-dihydro fused thiophene derivative as the core unit and 1,1-dicyanomethylene-3-indanone (IC) derivatives and different π -conjugated molecules other than IC as terminal acceptor units. All the investigated NFAs are found air-stable as the computed highest occupied molecular orbitals (HOMOs) are below the air oxidation threshold (ca. -5.27 eV vs. saturated calomel electrode). The studied NFAs can act as potential non-fullerene acceptor candidates as they are found to have sufficient open-circuit voltage (V_{oc}) and fill factor (FF) ranging from 0.62-1.41 eV and 83%-91%, respectively. From the anisotropic mobility analysis, it is noticed that the studied NFAs except dicyano-rhodanine terminal unit containing NFA, exhibit better electron mobility than the hole mobility, and therefore, they can be more promising electron transporting acceptor materials in the active layer of an organic photovoltaic cell. From the optical absorption analysis, it is noted that all the designed NFAs have the maximum absorption spectra ranging from 597 nm-730 nm, which lies in the visible region and near infra-red (IR) region of the solar spectrum. The computed light-harvesting efficiencies for the PM6 (thiophene derivative donor selected in our study): NFA blends are found to lie in the range of 0.9589-0.9957, which indicates efficient light-harvesting by the PM6:NFA blends during photovoltaic device operation.

INTRODUCTION

In recent years, acceptors have been at the forefront of organic-based photovoltaic research and development.^{1,2,3,4} So far, two types of acceptors have been extensively studied and they are fullerene acceptors (FAs) and non-fullerene acceptors (NFAs). Over the last few years, fullerene and its derivatives such as 6,6-phenyl-C₆₁-butyric acid methyl ester (PC₆₁BM), 6,6-phenyl-C₇₁-butyric acid methyl ester (PC₇₁BM), and indene-C₆₀ bisadduct (ICBA) played significant roles in boosting the organic photovoltaic performance as they all have a high electron affinity, unique spherical geometry, and good isotropic charge transport ability.^{5,6,7,8,9} However, their difficult and expensive synthesis, limited structural tunability, weak absorption spectra, and thermal instability become major bottlenecks for improving device performance.^{10,11,12} Alternatively, non-fullerene acceptors, namely 3,9-bis(2-methylene-(3-(1,1-dicyanomethylene)-indanone))-5,5,11,11-tetrakis(4-hexylphenyl)-dithieno[2,3-d:2',3'-d']-s-indaceno[1,2-b:5,6-b']dithiophene (ITIC), 2,2'-((2Z,2'Z)-((4,4,9,9-tetrahexyl-4,9-dihydro-s-indaceno[1,2-b:5,6-b']dithiophene-2,7-diyl)bis(methanylylidene))bis(3-oxo-2,3-dihydro-1H-indene-2,1-diylidene))dimalononitrile (IDIC), and 2,2'-((2Z,2'Z)-((12,13-bis(2-ethylhexyl)-3,9-diundecyl-12,13-dihydro-[1,2,5]thiadiazolo[3,4-e]thieno[2'',3'':4',5']thieno[2',3':4,5]pyrrolo[3,2-g]thieno[2',3':4,5]thieno[3,2-b]indole-2,10-diyl)bis(methanylylidene))bis(5,6-difluoro-3-oxo-2,3-dihydro-1H-indene-2,1-diylidene))dimalononitrile (Y6) have several advantages over fullerene acceptors such as easy synthesis, tunable energy levels via simple structural modifications, extended optical absorption profiles and favorable charge transfer at low energetic driving force while maintaining a good open-circuit voltage to short-circuit current density tradeoff.^{13,14,15} Non-fullerene acceptors typically contain different donor (D) and acceptor (A) blocks as core and terminal units, along with (possibly) π -bridging units with arrangements such as A-D-A, A- π -D- π -A, A₂-DA₁D-A₂. Different design strategies of core, terminal and bridging units, as well as their arrangements within the molecule, have led to promising NFAs for photovoltaic applications.^{13,16,17} In particular, structural tuning of core and terminal (or end) groups has been reported to be a promising strategy for building potential NFAs. For example, indacenodithiophene (IDT) is one of the most widely used cores in the NFA backbone. When the central benzene ring of the IDT core was substituted by naphthalene, the weaker electron-donating ability led to a blueshifted optical absorption, and the power conversion efficiency (PCE) of the devices having PBDB-T (donor):NFA reached up to 8-9%.^{18,19} In the IDT core, if the central benzene is replaced by an electron-rich thieno[3,2-*b*]thiophene (TT) unit, stronger intramolecular charge transfer (ICT) has been observed due to efficient π -electron delocalization.^{20,21} In addition, the stronger ICT broadened the absorption into the near-infrared (NIR) region, strong intermolecular interactions led to ordered molecular stacking, and the PCEs reached over 10% when matched with the PTB7-Th donor.^{20,21} In 2015, Lin *et al.* reported a NFA, namely ITIC, which achieved a PCE of up to 6.8% when blended with the PTB7-Th donor.²² Electron withdrawing fluorine atom substitution to the terminal 1,1-dicyanomethylene-3-indanone (IC) unit of ITIC leads to low-lying frontier molecular energy levels, a red-shifted absorption profile, and improved device efficiency.²³ Inspired by ITIC in 2017, Zou's group designed a new NFA named BZIC (dithieno[3,2-*b*]-pyrrolobenzotriazole-1,1-dicyanomethylene-3-indanone), having a nitrogen-atom-substituted core with a red-shifted optical absorption profile.²⁴ Combining the advantages of ITIC and BZIC, Yang's group designed the Y-series NFAs such as Y1, Y3, and Y6 (Y is an abbreviation for Yang).²⁵ The conjugation length of the nitrogen-atom-substituted core in BZIC is increased by thiophene ring incorporation in Y1, and

hence ICT is enhanced, and a red-shifted absorption spectrum was measured. Y3 was designed via terminal group modulation of Y1. Y1 contains 1,1-dicyanomethylene-3-indanone (IC), in which they substituted electron withdrawing fluorine (F) atoms, and the electronegativity of fluorine atoms in Y3 enhances ICT, broadens the optical absorption profile, and improves the molecular packing. In Y6, the central unit of the D-A-D core in BZIC, Y1, and Y3, i.e., benzotriazole (BTZ), is replaced by the stronger electron withdrawing benzothiadiazole (BT). In comparison to Y1 and Y3, Y6 showed superior morphology, high charge carrier mobility, low-lying highest occupied molecular orbital (HOMO) and lowest unoccupied molecular orbital (LUMO) levels, narrower bandgap, and a red-shifted absorption spectrum. The core and terminal modulation design strategy of crescent shaped Y series NFAs provides a PCE gain of 13.4% (Y1), 14.8% (Y3) to 15.7% (Y6), as well as an increase in fill factor from 69.1% (Y1), 71.2% (Y3) to 74.8% (Y6).²⁵ Recently, the highest efficiency for single junction organic solar cells is reported as 18.22%, where the active layer is composed of D18 polymer donor and Y6 non-fullerene acceptor.²⁶ Khan *et al.* computationally designed new Y-series near-infrared sensitive NFAs based on reported Y21 acceptor (asymmetric core D-A-D unit) via terminal group modulation.²⁷ They found that terminal unit variation reduced the frontier molecular orbital energy levels, reorganization energy, exciton binding energy, as well as improved the absorption maximum and open-circuit voltage. Recently, Li and his group theoretically designed a series of six NFAs (Y6-COH, Y6-COOH, Y6-CN, Y6-SO₂H, Y6-CF₃, and Y6-NO₂). They replaced the electronegative fluorine (F) atoms on the terminal fluorinated IC unit of Y6 with different electron-withdrawing end groups (-COH, -COOH, -CN, -SO₂H, -CF₃, -NO₂).²⁸ They observed that among the end-capped engineered NFAs, Y6-NO₂ has the lowest-lying frontier molecular orbitals and the largest red-shifted absorption profile; moreover, the PM6 (donor)/Y6-NO₂ (NFA) complex system showed stronger interfacial interactions and enhanced charge-transfer (CT) characteristics as compared to the PM6/Y6 composite.²⁸ In 2019, inspired by the excellent Y-series NFAs, Zhou *et al.* introduced a quinoxaline moiety core replacing the benzothiadiazole core of Y6 and designed two Y-series molecules namely, AQx-1 and AQx-2.²⁹ The quinoxaline moiety is reported to have the quinoid-resonance effect, and the reduced free σ -bonds in AQx could lower the reorganization energy and improve the electron transport and intermolecular packing. They achieved a device efficiency of 16.64% with significant short-circuit current density and fill factor for the binary organic solar cells containing AQx-2 as NFA and PBDB-TF (PM6) as donor.²⁹ While the Y-series NFAs have been widely used as active layer components in bulk-heterojunction organic solar cells, and ternary solar cells, there is still considerable room for improvement in non-fullerene acceptors.

In our study, we have modified the recently reported AQx-2 by designing a NFA namely **AQx-2-c** in which quinoxaline core of AQx-2 is replaced by 2,3-quinoxalinedione,1,4-dihydro, which has a weaker electron donating ability than quinoxaline. Further, we performed terminal unit engineering of **AQx-2-c** (terminal unit: Fluorinated IC) with various halogen substituted, π -extended, and thieryl fused IC groups as well as explored end-capped groups different than IC.^{16,30} Thus, we proposed eight new NFAs namely **AQx-2-ct1** (terminal unit: Chlorinated IC), **AQx-2-ct2** (terminal unit: Fluorinated naphthyl fused IC), **AQx-2-ct3** (terminal unit: Chlorinated naphthyl fused IC), **AQx-2-ct4** (terminal unit: γ -thienyl IC), **AQx-2-ct5** (terminal unit: β -thienyl IC), **AQx-2-ct6** (terminal unit: Rhodanine), **AQx-2-ct7** (terminal unit: Dicyano-Rhodanine), and **AQx-2-ct8** (terminal unit: Malononitrile). We studied computationally the geometrical, optoelectronic, intra and intermolecular charge transport properties, and overall photovoltaic performance of the designed crescent-shaped NFAs using density functional theory

(DFT) and time-dependent DFT (TD-DFT). In the present study, Poly[(2,6-(4,8-bis(5-(2-ethylhexyl-3-fluoro)thiophen-2-yl)-benzo[1,2-*b*:4,5-*b'*])dithiophene))-alt-(5,5-(1',3'-di-2-thienyl-5',7'-bis(2-ethylhexyl)benzo[1',2'-*c*:4',5'-*c'*])dithiophene-4,8-dione)] (PM6) is selected as the donor as it has well matched frontier molecular orbitals with respect to the designed NFAs. The absorption properties as well as charge transfer analysis of the PM6 donor and designed NFAs blends or complexes have been investigated.

COMPUTATIONAL METHODOLOGY

Within the framework of density functional theory, benchmarking a suitable functional to obtain satisfactory agreement with the experimental results available from cyclic voltammetry, and ultraviolet photoelectron spectroscopy measurements has been a difficult task.^{28,31,32} In our present study, we optimized the reference NFA, AQx-2 (Figure 1) using different functionals (B3LYP, B3LYP-D3BJ, PBE0, MPW91PW91, M06, and ω B97XD).^{33,34,35,36,37,38} coupled with the 6-31G(d,p) and 6-311G(d,p) basis sets to compute the highest occupied molecular orbital (HOMO). The computed HOMO energy (-5.52 eV) of AQx-2 using B3LYP-D3BJ/6-31G(d,p) as listed in Table S1 in the supporting information (SI) was found to be in good agreement with the experimentally reported value (-5.62 eV). The B3LYP functional has been used to optimize the ground state geometries of crescent shaped Y-series NFAs, and the computed HOMO energy is usually found to be in good agreement with experimentally reported results.^{28,39,40} From Table S1, the computed HOMO energy is, perhaps not surprisingly, almost the same for B3LYP and B3LYP-D3BJ. Therefore, in our study, the ground state geometries of the designed NFAs (Figure 2) are optimized using the dispersion-corrected B3LYP-D3BJ functional in conjunction with the 6-31G(d,p) basis set in the gas phase. The ground state geometry of the PM6 donor has been determined at the same theoretical level and the highest occupied molecular orbital (HOMO) and lowest unoccupied molecular orbital (LUMO) energies as well as optical band gap ($E_{g,opt}$) are determined by linear extrapolation to $n = \infty$ from the explicit computations on PM6 systems with $n=1-4$ monomer units (Figure S1, Table S2). The optimized geometries of the studied NFAs and PM6 donor were confirmed as minima by carrying out vibrational frequency analysis, which yielded real harmonic frequencies. For all the studied compounds, the full alkyl chains were retained in calculations.

Further, to choose a reasonable computational level to simulate the optical absorption properties of the investigated NFAs, the maximum absorption wavelength of the reference AQx-2 acceptor (at the B3LYP-D3BJ optimized geometry) was computed using different hybrid (B3LYP-D3BJ, PBE0, M06) and long-range corrected functionals (LC- ω PBE, LC-BLYP, CAM-B3LYP, ω B97XD) in conjunction with the 6-31G(d,p) basis set in Chloroform solvent medium, such that comparison could be made to the reported experimental values of Zhou *et al.*²⁹ The excitation energies and corresponding oscillator strengths were determined within the framework of TD-DFT alongside the integral equation formalism polarizable continuum (IEF-PCM) model to treat solvation. The simulated maximum absorption wavelength of AQx-2 using the B3LYP-D3BJ/6-31G(d,p) theoretical level was close to the experimental result (Table S3). A similar observation was reported earlier for crescent shaped Y-series NFAs.^{27,28} Hence, optical absorption spectra of the structurally similar NFAs investigated here are computed at the B3LYP-D3BJ/6-31G(d,p) theoretical level. Usually, the computed LUMOs at the DFT level differ significantly from experimentally reported values. Therefore, in our study, to predict

reliable LUMO energies, we use $E_{LUMO} = E_{HOMO} + E_{g,opt,TD}$, where $E_{g,opt,TD}$ is the optical band gap, evaluated from TD-DFT analysis.^{31,32} The reorganization energy, ionization potential, and electron affinity of all the designed NFAs are computed at the B3LYP-D3BJ/6-31G(d,p) level of theory. Crystal structures of the designed NFAs have been predicted employing the most reliable Dreiding force field within the Polymorph Predictor module of the BIOVIA Materials Studio17 based on their optimized gas-phase conformations.⁴¹ All possible crystal structures are selected by energy minimization of crystals with the most common space groups such as $P2_1/C$, $P1$, $P1$, $Pbca$, $P2_12_12_1$, $P2_1$, $C2/c$, $Pna2_1$, Cc , $Pbcn$, and $C2$.^{4,42,43,44,45} Crystal structure prediction method within the Polymorph Predictor module relies on Monte Carlo simulation which is a stochastic process. To assess the completeness of the search within this module, we have repeated the simulations for several times for each initial molecular structure until the same low energy crystal structures are produced. We generated large number of possible polymorphs using Dreiding force field parametrization which is considered to be a reasonable choice for organic molecules.^{4,43,44,45} The charge transfer integrals of the designed NFAs are evaluated using the site energy correction method at the PW91/TZP level of theory using the ADF program.^{46,47} The PW91/TZP theoretical level has been widely used to evaluate charge transfer integrals of organic molecules.^{48,49,50} Further, to model the interface between the PM6 donor and the NFAs, we performed end-to-end acceptor-acceptor (A-A) stacking. In the A-A stacking, the stacking occurs between the electron-withdrawing end groups of the NFAs and the electron withdrawing unit (A) of the polymer PM6 donor. For simplification, only one repeat unit of the polymer donor PM6 was considered in our study, and unsaturated atoms were hydrogenated. The geometry of the bimolecular system (PM6:NFA) is optimized using the computationally efficient extended tight-binding (GFN2-xTB) method.⁵¹ To investigate the intermolecular charge transfer (CT) states of the PM6-NFA complexes, natural transition orbital (NTO) analysis and interfragment charge transfer (IFCT) have been performed using TD-DFT. The NTO and IFCT analysis have been done using the range-separated functional CAM-B3LYP (with the 6-31G(d,p) basis set), as this approach has been widely accepted for calculating the intermolecular CT properties of such donor/acceptor complex systems.^{2,52,53} The NTO analysis, transition density matrix (TDM), and charge density difference (CDD) calculations reported in this study were done using Multiwfn 3.8 (dev).⁵⁴ Unless otherwise noted, all the DFT and TD-DFT calculations were carried out using the Gaussian 16 program.⁵⁵

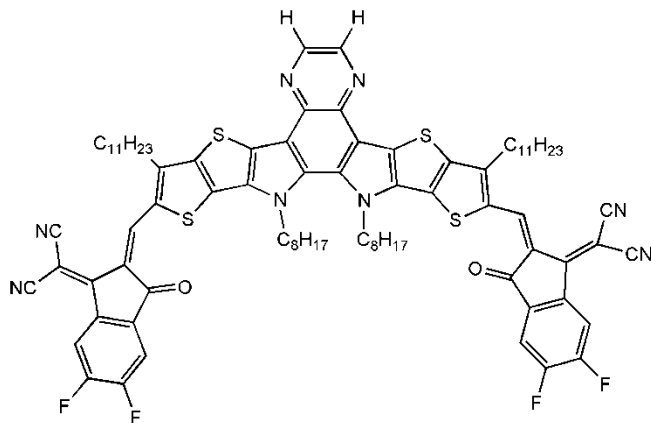


Figure 1: Molecular structure of the reference non-fullerene acceptor AQx-2.²⁹

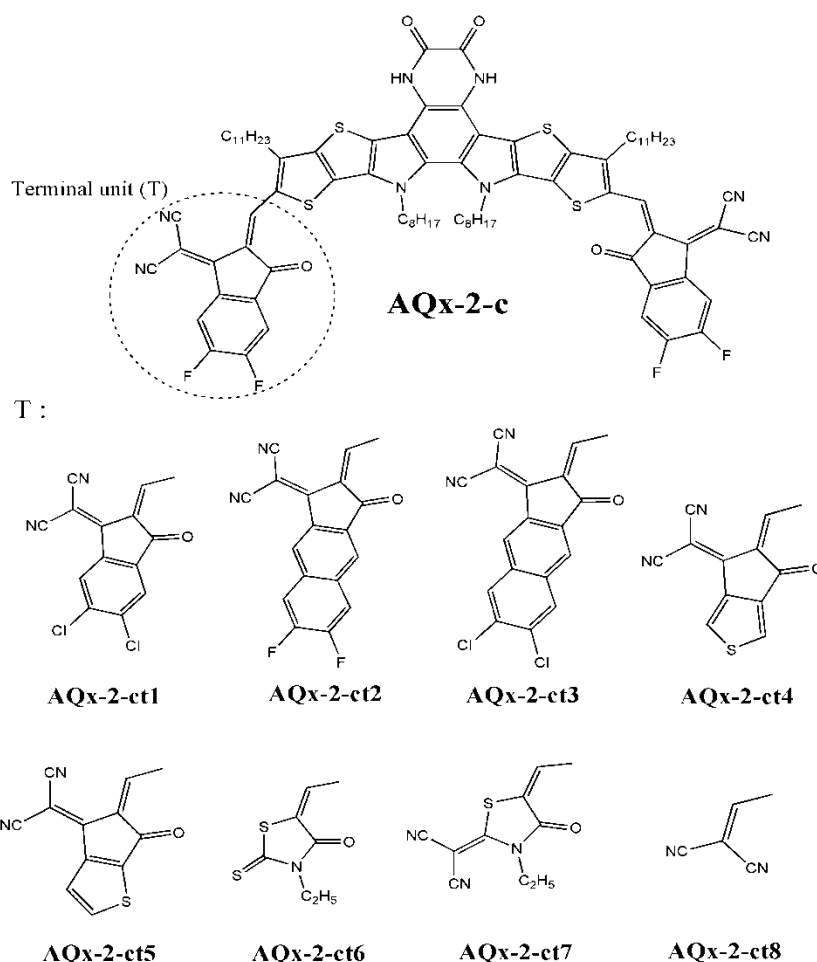


Figure 2: Chemical structures of the designed NFAs.

RESULTS AND DISCUSSIONS

Molecular Geometries and Molecular Electrostatic Potential (MEP) of the Designed NFAs.

The chemical structures of the designed NFAs are shown in Figure 2. Important geometrical parameters related to NFA functionality involve the bond lengths (d_1 , d_2 , d_3 , d_4) and dihedral angles (α , β , γ) and they have been shown in Figure 3; the optimized parameters are summarized in Table S4. The dihedral angle γ (Figure 3) denotes the planarity of the core D-A₁-D unit, and α , β represents the dihedral angles between the center donor unit and two terminal acceptor units. For all the designed NFAs except **AQx-2-ct8**, α (range: 1.31-1.45°), β (range: 1.83-1.96°), and γ (range: 1.68-1.94°) values are almost zero indicating the near planarity of the acceptors. It is also observed that all the newly designed NFAs have a modestly more planar core than the reference AQx-2 as they have smaller γ values compared to AQx-2 (ca 2° vs 3°). The computed bond lengths range from 1.37 Å to 1.42 Å, that falls between the carbon-carbon single bond length (C-C = 1.54 Å) and the carbon-carbon double bond length (C=C = 1.33 Å). Therefore, all

the bonds exhibit significant double bond character, which facilitates the delocalization of π -electrons over the whole molecular backbone and, importantly, this effective π -conjugation increases the charge transport properties.¹

To realize the variation of electron density over the molecular backbone of the designed NFAs, molecular electrostatic potential (MEP) analysis has been carried out (Figure S2). The MEP plots represent different values of the electrostatic potential in terms of different colors where the negative potential increases on moving from blue to red as blue < green < yellow < orange < red. For **AQx-2-c**, the core A₁ unit is more electronegative as it contains electron rich oxygen atom rather than hydrogen in reference NFA AQx-2 (Figure S2). For **AQx-2-c** and other designed NFAs, the negative potential is concentrated mostly on the core unit and the positive potential on the whole conjugated backbone and on the terminal units. Therefore, the separation between the negative and positive regions is more prominent for our designed NFAs than the reference AQx-2 which indicates delocalization of the π -electrons over the molecular backbone.

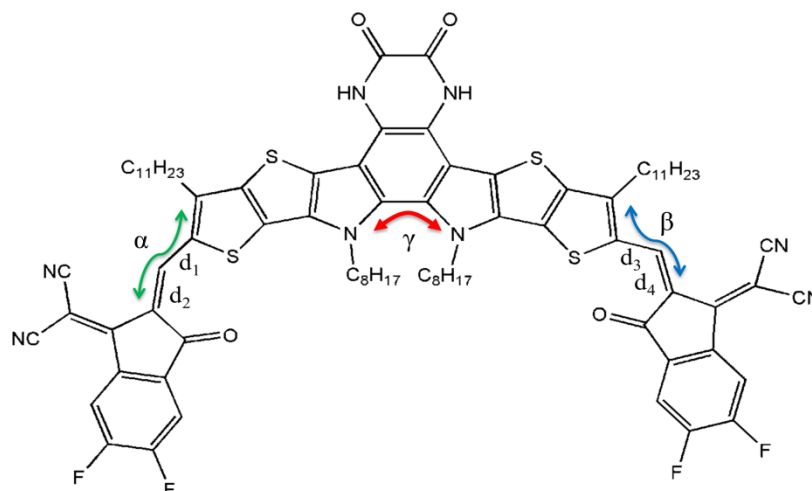


Figure 3: Representation of dihedral angles (α , β , γ) and bond lengths (d_1 , d_2 , d_3 , d_4) in a NFA (**AQx-2-c**).

Electronic Properties and Air-stability.

The energies of frontier molecular orbitals, i.e., the HOMO and LUMO energies, are significant factors for estimating the air-stability, optoelectronic, charge transfer, and photovoltaic properties of organic molecules. The HOMO values of the designed NFAs are computed at the B3LYP-D3BJ/6-31G(d,p) level of theory in the gas phase. The LUMO energies are predicted at the same theoretical level in the gas phase using the indirect approach, as discussed in computational methodology section. For organic molecules to be air-stable, the HOMO energy should be below the air oxidation threshold (ca. -5.27 eV or 0.57 V vs. saturated calomel electrode (SCE)).⁵⁶ In our present study, the computed HOMO levels of the investigated designed NFAs range from -5.28 to -5.77 eV (Figure 4), and hence, they should possess ambient stability under atmospheric conditions. All the designed NFAs, except **AQx-2-ct6**, possess

deeper HOMO energies than that of reference AQx-2, and therefore, they are more air-stable than AQx-2. The chlorine atom has a stronger electron-withdrawing ability than fluorine, and therefore, both **AQx-2-ct1** (1.78 eV) and **AQx-2-ct3** (1.76 eV) show narrow band gaps and downshifted HOMO/LUMO energies compared to their fluorinated counterparts **AQx-2-c** (1.82 eV) and **AQx-2-ct2** (1.79 eV). The NFA with thienyl fused IC terminal units, **AQx2-ct4** (1.82 eV), exhibits a modestly smaller band gap than AQx-2 (1.85 eV). In **AQx-2-ct7**, the electron-withdrawing cyano group in the Rhodanine terminal group leads to low-lying HOMO and LUMO energies and results in improved air-stability as well as a slightly narrowed-band gap acceptor as compared to **AQx-2-ct6**. From Figure 4, the HOMO and the LUMO energies of the designed NFAs are lower-lying than those of the donor PM6 polymer, and hence, they can receive negatively charged electrons from or deliver positively charged holes to the PM6 polymer donor. The contours of the frontier molecular orbitals (FMOs) are shown in Figure S3 and Figure S4, and for all the designed NFAs, the HOMOs are delocalized over the entire conjugated molecular backbone, which suggests free electron availability and potential charge transport capacity. In contrast, the LUMO electron density localizes predominantly on the terminal acceptor units of the designed NFAs, and that indicates transportation of electrons from the core D-A₁-D unit to the terminal A₂ units. For an n-type air-stable organic molecule, the LUMO energy must approach approximately -4.0 eV to ensure good coupling with the cathode electrode material, such as Gold (Au) or Aluminum (Al).⁵⁷ The computed LUMO levels of the designed compounds range from -3.19 eV to -3.98 eV. Except for **AQx-2-ct6**, all the designed NFAs have more n-type character. In general, for organic solar cell devices, Aluminum (workfunction, $\Phi = -4.3$ eV) is selected as the cathode electrode material, and, thus, the charge (hole and electron) injection barriers of the investigated NFAs are computed with respect to the Aluminum (Al) electrode (Table S5). The electron injection barriers of the NFAs except **AQx-2-ct6** are significantly less than the corresponding hole injection barriers indicating n-characteristics of the studied NFAs. The electron injection barriers of the designed NFAs, except **AQx-2-ct5** to **AQx-2-ct8** are less than that for the reference NFA, AQx-2, i.e., 0.32-0.49 eV < 0.63 eV; and thus **AQx-2-c** and **AQx-2-ct1** to **AQx-2-ct4** will couple well with an Al electrode. As a result, those NFAs may favor better electron injection than AQx-2.

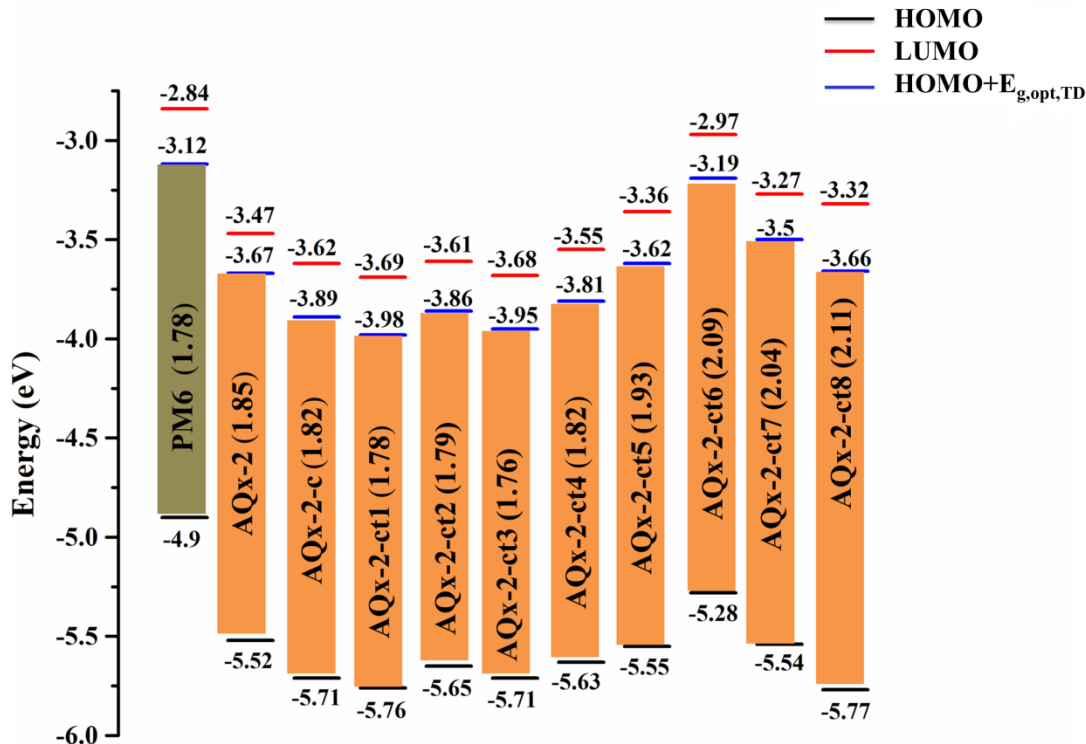


Figure 4: HOMO and LUMO (DFT and TDDFT both with B3LYP-D3BJ/6-31G(d,p)) energies of the designed NFAs and PM6 donor in the gas phase.

Table 1: Computed open-circuit voltage (V_{oc}), Fill Factor (FF), Energetic Driving Force (L_D-L_A) Between PM6 Donor and Designed NFAs at B3LYP-D3BJ/6-31G(d,p) Level of Theory

Comp.	V_{oc} (V)	FF (%)	L_D-L_A (eV)
AQx-2 (Ref.)	0.93	87	0.55
AQx-2-c	0.71	85	0.77
AQx-2-ct1	0.62	83	0.86
AQx-2-ct2	0.74	85	0.74
AQx-2-ct3	0.65	84	0.83
AQx-2-ct4	0.79	86	0.69
AQx-2-ct5	0.98	88	0.50
AQx-2-ct6	1.41	91	0.07
AQx-2-ct7	1.10	89	0.38
AQx-2-ct8	0.94	88	0.54

Open-circuit Voltage (V_{oc}), Fill Factor, and Energetic Driving Force.

The key photovoltaic parameters of an organic solar cell, including open-circuit voltage (V_{oc}), fill factor (FF), short-circuit current density (J_{sc}), and driving force energy (L_D-L_A) are highly correlated with the HOMO and LUMO values of the donors and acceptors. The open circuit

voltage V_{oc} for the studied NFAs are estimated from the empirical equation proposed by Scharber *et al.*,⁵⁸

$$V_{oc} = \left(\frac{1}{e}\right)(|E_{HOMO}(D)| - |E_{LUMO}(A)|) - 0.3 V \quad (1)$$

Here e is the elementary charge, $E_{HOMO}(D)$ is the HOMO level of the donor (D) and $E_{LUMO}(A)$ is the LUMO level of the acceptor (A). The empirical factor, 0.3 V represents losses in transport to the electrodes.⁵⁸ It is evident that a deeper HOMO level of the donor combined with a shallower LUMO level of the acceptor leads to high V_{oc} . For example, **AQx-2-c** has an upshifted LUMO energy compared to its chlorinated counterpart **AQx-2-ct1**, and, hence, **AQx-2-c** has a higher V_{oc} (0.71 eV) than **AQx-2-ct1** (0.62 V). Similarly, the LUMO energy is found to be higher for **AQx2-ct5** having β -thienyl IC terminal group than **AQx-ct4** (terminal unit: γ -thienyl IC), and that leads to higher V_{oc} for **AQx2-ct5** (0.98 V) as compared to **AQx-2-ct4** (0.79 V). It is reported that during the photo-oxidation process in blend films, NFAs having low-lying LUMO levels could suppress the charge transfer between NFAs and oxygen, and that leads to quenching photo-oxidation for both donors and acceptors in blend films, which is important for the stability of NFAs.²⁸ In this present study, among all the designed NFAs, **AQx-2-c**, **AQx-2-ct1**, **AQx-2-ct2**, **AQx-2-ct3**, **AQx-2-ct4**, **AQx-2-ct5**, **AQx-2-ct8** have lower-lying LUMO energies, and therefore, they have excellent photo-oxidation stability but relatively smaller V_{oc} . Nevertheless, the computed V_{oc} s of the designed NFAs as listed in Table 1 range from 0.62-1.41 eV. The computed V_{oc} for the reference NFA AQx-2 is 0.93 V, which is slightly overestimated relative to the reported experimental value (0.86 V).²⁹ This slight deviation between computed and measured values is reasonable because experimentally V_{oc} depends on energy levels as well as temperature, light source, charge-carrier recombination, light intensity, and morphology of the photovoltaic device.¹

The fill factor (FF) is one of the essential parameters that affect the power conversion efficiency of the organic photovoltaic device. However, series resistance (R_s) and shunt resistance (R_{sh}) are the two critical factors that influence the FF.⁵⁹ For organic materials, theoretical prediction of the R_s and R_{sh} is still a challenging task. Therefore, in ideal condition, FF can be expressed as^{60,61},

$$FF = \frac{\gamma_{oc} - \ln(\gamma_{oc} + 0.72)}{\gamma_{oc} + 1} \quad (2)$$

Here, γ_{oc} is defined as dimensionless voltage:

$$\gamma_{oc} = \frac{eV_{oc}}{k_B T} \quad (3)$$

In this equation, e , V_{oc} , k_B , and T denote elementary charge, open-circuit voltage, Boltzmann constant and temperature (300 K), respectively. The accuracy of the equation holds for $\gamma_{oc} > 10$.^{60,61} The calculated γ_{oc} values for the studied NFAs are found to be greater than 10. The computed fill factor values are listed in Table 1. The FF is linearly correlated with the V_{oc} , and therefore, the NFAs having upshifted LUMO levels have comparatively higher FF.^{59,60,61} The computed fill factor for AQx-2 is 87%, which is slightly overestimated compared to the reported experimental reported value (76%).²⁹ In practical operating conditions, various loss mechanisms also take place, which are neglected during the theoretical estimation of the FF values.⁶¹ Therefore, the computed FF values are usually found to be overestimated, but the predicted trends are expected to be the similar.

In our study, the calculated LUMO-LUMO offsets or the energetic driving forces (L_D-L_A), i.e., the LUMO energy differences between the donor and acceptor are listed in Table 1. The NFAs having upshifted LUMO levels possess low energetic driving forces. Therefore, they may facilitate the fast exciton dissociation process at the donor/acceptor interface as compared to others with higher LUMO-LUMO offsets.

Optical Absorption Properties.

The short-circuit current density (J_{sc}) is a crucial figure of merit for organic photovoltaic devices, and it is greatly influenced by the intensity and range of the optical absorption spectrum.^{31,62,63} The short-circuit current density (J_{sc}) is defined as^{62,63}

$$J_{sc} = q \int \eta_{EQE}(\lambda) S(\lambda) d\lambda \quad (4)$$

where $S(\lambda)$ denotes the photon number over all frequencies. The external quantum efficiency (η_{EQE}) appearing in Eq. (4) can be determined as the product of four physical parameters: the light harvesting efficiency (η_λ), exciton-diffusion efficiency (η_{ED}), charge transfer efficiency (η_{CT}) and charge-collection efficiency (η_{CC}),^{62,64} i.e.,

$$\eta_{EQE} = \eta_\lambda \eta_{ED} \eta_{CT} \eta_{CC} \quad (5)$$

The light harvesting efficiency (η_λ) is associated with the oscillator strength (f) of the corresponding excitation with wavelength (λ) as³¹:

$$\eta_\lambda = 1 - 10^{-f} \quad (6)$$

The computed optical absorption parameters of the investigated NFAs at the B3LYP-D3BJ/6-31G(d,p) level of theory in the solvent (Chloroform) phase are summarized in Table S6; values are provided for the two highest oscillator strengths values. The simulated optical absorption spectra including the lowest 20 excited states are depicted in Figure 5. About 70% of the solar photon flux is within the wavelength region 380 nm to 900 nm. Therefore, a promising NFA should have strong absorption in this region to harvest more photons, enhancing J_{sc} . In

photovoltaic cells, both the donor and acceptor contribute to light absorption with photoexcitations generated in their respective domains. The donor PM6 polymer is reported to absorb light in the UV-visible region.^{28,65,66} In our study, it is found that all the designed NFAs have the maximum absorption spectra ranging from 597 nm-730 nm, which falls in the visible region to near infra-red (IR) regions of the solar spectrum. The optical absorption spectrum of a molecule strongly depends on the nature of the different substituents in the conjugated backbone. For example, **AQx-2-ct1** has a red-shifted absorption spectrum compared to **AQx-2-c** as the former has more electron withdrawing Cl atoms at its terminal ends. This observation is also valid for **AQx-2-ct2** and **AQx-2-ct3**. In between, the NFAs with thienyl fused IC terminal units, **AQx-2-ct4** having γ -thienyl has a smaller optical band gap and hence exhibits a red-shift in its absorption spectrum. Also, in **AQx-2-ct7**, the electron-withdrawing cyano group in the Rhodanine terminal group leads to narrow optical band gap acceptors and displays red-shifted absorption compared to Rhodanine containing **AQx-2-ct6**. Among the designed NFAs, **AQx-2-ct3** shows the largest red-shift having the maximum absorption wavelength of 730 nm as it has an extended π -conjugated terminal unit containing the electron withdrawing -Cl atoms. The NFAs, **AQx-2-ct5**, **AQx-2-ct6**, **AQx-2-ct7**, and **AQx-2-ct8**, have blue-shifted absorption profiles compared to **AQx-2-c** because of their higher band gaps. The short-circuit current density is proportional to the light harvesting efficiency (η_λ). In the present study, the light harvesting efficiency is computed for the brightest excited state transition having the largest oscillator strength. Among all the designed compounds, light harvesting efficiencies for **AQx-2-c**, **AQx-2-ct1**, **AQx-2-ct2**, **AQx-2-ct3**, and **AQx-2-ct4** are slightly higher (~1-2 %) than the other designed NFAs.

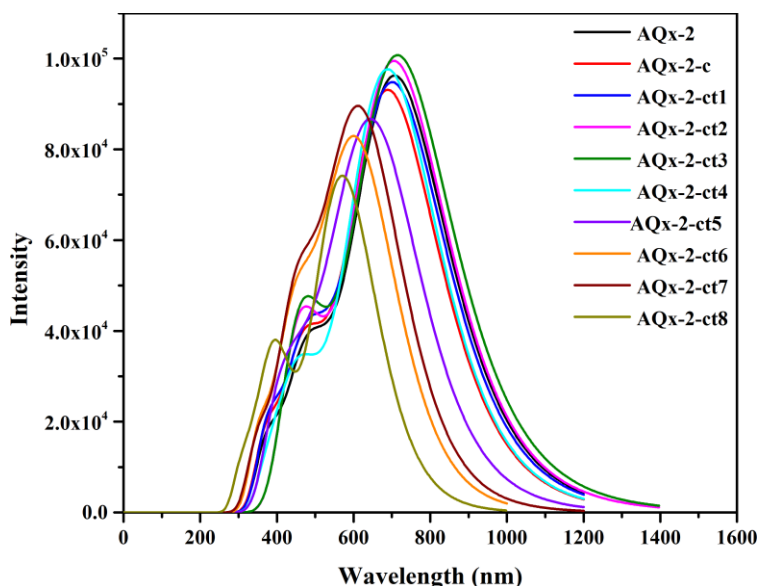


Figure 5: Simulated absorption spectra of the designed NFAs in the solution phase (Chloroform) at the B3LYP-D3BJ/6-31G(d,p) level of theory. Spectra include the lowest 20 excitations with Gaussian line shape with peak half-width at half height: 0.333 eV.

Intramolecular Charge Transport Properties, Electron/Hole Distribution and Transition Density Matrix.

To investigate the intramolecular charge transport properties of the designed NFAs, the electron/hole distributions of the first bright excited states are computed at the CAM-B3LYP/6-31G(d,p) level of theory level in Chloroform solvent based on gas-phase B3LYP-D3BJ/6-31G(d,p) optimized geometries.^{67,68} To understand the electron-hole localization, spatial span, and the primary sites of the singlet excited state electron-hole bound excitons, transition density matrix (TDM) analysis has been performed.^{69,70,71} Several different measures of intramolecular charge transport properties are considered: (a) simulated charge density difference ($\Delta\rho$) plots associated with the $S_0 \rightarrow S_1$ transition, (b) the extending zones of the centroids C+ (positive region)/C- (negative region) associated with $S_0 \rightarrow S_1$ transition, and (c) transition density matrix (TDM) analysis. These are illustrated in Figure 6 for the parent **AQx-2-c** compound; results for all the designed NFAs can be found in supplementary information Figures S5-S8. Upon visual inspection, the plots for all the designed NFAs are qualitatively similar to their parent **AQx-2-c**. From the charge density difference (CDD) analysis, the intramolecular charge transfer amounts (q_{CT}) of the reference AQx-2 and studied NFAs do not change significantly (0.61-0.67 $|e^-|$) (Table 2), which suggests that the structural modulation of both the core and the terminal units has a small impact on q_{CT} . However, the intramolecular charge transition distance (D_{CT}) and the variation of dipole moment ($\Delta\mu_{CT}$) between the ground and excited state of the designed NFAs vary significantly. From Table 2, it is clear that the D_{CT} increases slightly after core and terminal unit substitution of the reference NFA AQx-2. The fact is also supported by the computed $\Delta\mu_{CT}$ values. Among the designed NFAs, **AQx-2-ct3** and **AQx-2-ct2** have larger D_{CT} and higher $\Delta\mu_{CT}$ than others due to their longer π -conjugated molecular backbone. This observation also suggests that after local excitation, the intramolecular charge recombination of **AQx-2-ct3** and **AQx-2-ct2** should be more difficult, and charge transfer may be easier than for the other designed NFAs.

The hydrogen atoms have insignificant contribution to the transitions, and, therefore, in our present study, the hydrogen atoms are omitted in Figure 6c and the correlation between the atomic indices of the NFAs and the labels of the TDM plots are shown in Figure S9.⁵⁴ The reference NFA and our designed NFAs have the similar A_2 - DA_1 D- A_2 molecular structures, and, thus, the molecular backbone is subdivided into three parts the terminal electron withdrawing unit (A_2), the core unit (D), and the central electron withdrawing part (A_1). All the simulated TDM maps show similar behavior where the electron coherence mainly appears at the D parts and the terminal A_2 parts. The excitations found in the TDM maps are delocalized over the whole molecular backbone, which is consistent with Figure 6a; compare also Figures S5-S8. The dark sites in these TDM plots are from side alkyl chains, which are not involved in the excitations. From the electron-hole correlation found along the diagonals, during the excitation process, the electrons slightly migrate from the D to the terminal acceptor (A_2) part, which is supported by the localization of the LUMO density on terminal units as depicted in Figures S3 and S4.

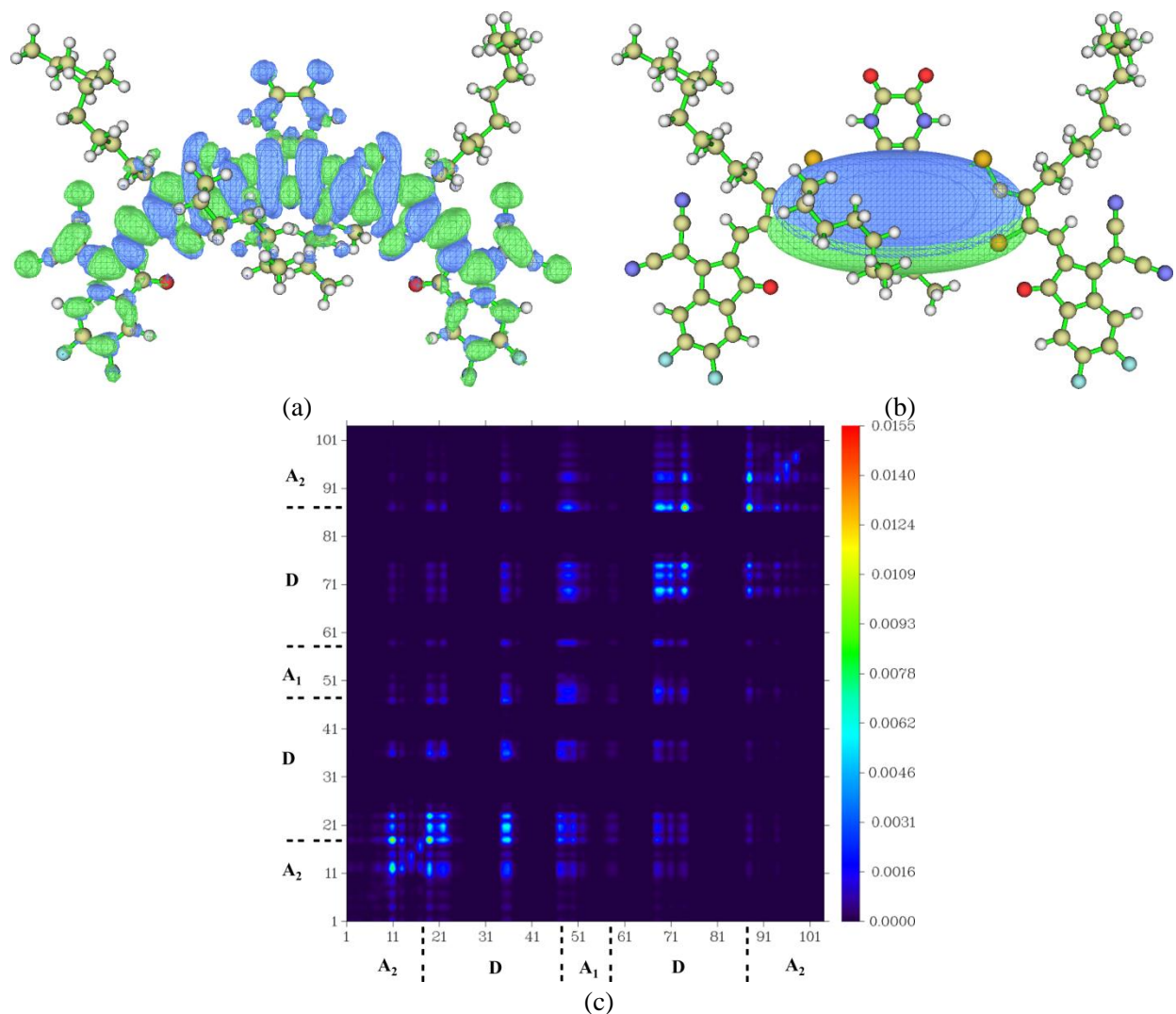


Figure 6: Simulated (a) charge density difference ($\Delta\rho$) plots, (b) extending zones for the centroids C+/C-, and (c) transition density matrix (TDM) associated with the $S_0 \rightarrow S_1$ transition of the studied NFA (AQx-2-c) at the CAM-B3LYP/6-31G(d,p) level of theory in Chloroform solvent. The green and blue regions in (a) and (b) correspond to positive and negative regions, respectively and the isosurface value is 0.0002 a.u. In (c), the hydrogen atoms of all molecular systems are omitted and the color bars are given on the right.

Table 2. Transferred Charges (q_{CT}), Charge Transfer Distance (D_{CT}), and Variation of Dipole Moments ($\Delta\mu_{CT}$) for the Transition $S_0 \rightarrow S_1$ at the CAM-B3LYP/6-31G(d,p) Level of Theory in Chloroform Solvent

Comp.	q_{CT} (e^-)	D_{CT} (Å)	$\Delta\mu_{CT}$ (Debye)
AQx-2 (ref)	0.65	1.137	3.564
AQx-2-c	0.66	1.249	3.993
AQx-2-ct1	0.67	1.317	4.226
AQx-2-ct2	0.67	1.410	4.523
AQx-2-ct3	0.67	1.484	4.777
AQx-2-ct4	0.66	1.337	4.215
AQx-2-ct5	0.67	1.193	3.859
AQx-2-ct6	0.63	1.380	4.189
AQx-2-ct7	0.64	1.362	4.233
AQx-2-ct8	0.61	1.159	3.410

Electron Affinity (EA), Ionization Potential (IP), Mulliken electronegativity (ME) and Reorganization energy.

The ionization potentials (IPs), electron affinities (EAs), and reorganization energies play important roles in the charge transport mechanism in organic molecules. The adiabatic and vertical ionization potentials, as well as electron affinities, are listed in Table 3. The computed values of adiabatic EA for all the designed NFAs except **AQx-2-ct6**, are found to be higher than 2.4 eV, suggesting their air-stability and n-type characteristics.^{72,73} The fact is also supported by the shallow LUMO energy of **AQx-2-ct6**, as discussed in electronic properties and air-stability Section. The computed values of the Mulliken Electronegativity (ME) are also listed in Table 3. The Mulliken electronegativity is calculated as half of the sum of the vertical ionization potential (IP(v)) and the vertical electron affinity (EA(v)) energy. A molecule having a larger Mulliken electronegativity index possesses a higher electron withdrawing ability⁷⁴, and, thus, all the designed NFAs, except **AQx-2-ct5**, **AQx-2-ct6**, and **AQx-2-ct7**, have larger electron withdrawing ability than the reference AQx-2. In the present study, the contribution of the external reorganization energy (λ_{ext}) is neglected as the contribution of λ_{ext} is expected to be less sensitive to the chemical structure.^{75,76,77} The internal reorganization (λ_i) energies of all the investigated NFAs during hole and electron transfer are evaluated using the adiabatic potential energy surface (APS) method as described in Section S.2.3 in the supporting information.⁷⁸ From Table 3, the electron reorganization energy (λ_e) is significantly lower than the hole reorganization energy (λ_h) for all the designed NFAs except for **AQx-2-ct6** and **AQx-2-ct7**. The NFAs having lower λ_e than λ_h should be better for electron transport. For **AQx-2-ct8**, both values of λ_e and λ_h are almost the same, and, hence, it may have balanced hole and electron transport rates. Moreover, the charge transport efficiency also depends on the charge transfer integral, which is influenced by molecular packing.

Table 3. Hole/electron Reorganization energies (λ_h/λ_e), Adiabatic/Vertical Ionization Potential (IP(a)/IP(v)), Adiabatic/Vertical Electron Affinity (EA(a)/ EA(v)) and Mulliken Electronegativity (ME) in eV of the studied NFAs

Comp.	λ_h	λ_e	IP(a)	IP(v)	EA(a)	EA(v)	ME
AQx-2 (Ref.)	0.176	0.132	6.22	6.31	2.77	2.70	4.50
AQx-2-c	0.177	0.132	6.42	6.51	2.92	2.85	4.68
AQx-2-ct1	0.175	0.122	6.46	6.54	3.01	2.95	4.74
AQx-2-ct2	0.170	0.115	6.33	6.41	2.94	2.88	4.65
AQx-2-ct3	0.168	0.106	6.37	6.46	3.02	2.97	4.72
AQx-2-ct4	0.168	0.127	6.34	6.43	2.84	2.78	4.60
AQx-2-ct5	0.183	0.137	6.27	6.36	2.64	2.58	4.47
AQx-2-ct6	0.182	0.197	6.02	6.11	2.24	2.14	4.13
AQx-2-ct7	0.172	0.204	6.26	6.34	2.56	2.46	4.40
AQx-2-ct8	0.166	0.170	6.60	6.68	2.49	2.41	4.54

Crystal Structure Prediction, Charge Transfer Integral, and Anisotropic Mobility.

For every NFA, including the reference compound AQx-2, the structure with the lowest lattice energy from the considered space groups has been selected for further calculations. The simulated unit cell parameters of the lowest energy space group for all the NFAs are given in Table S7. The simulation details are mentioned in Section S1 in the Supporting Information. The packing motifs of all the investigated NFAs are found to be π -stacked parallel, where example are shown for AQx-2, **AQx-2-c** and **AQx-2-ct3** in Figure 7; all other packing structures can be found in SI (Figure S10-S12). Based on the predicted crystal structures, we consider one molecule in a crystal as the center, and its adjacent parallel dimers are represented as D1-D8. The rate of charge transfer (K) are calculated using Marcus theory (as described in Section S.2.1 in the Supporting Information) along different pathways, as depicted in Figures 7 and S10-S12.^{78,79,80} The charge transfer integral or intermolecular electron coupling (V) is one of the key parameters influencing the charge carrier mobility, and it is determined by the orbital coupling of the adjacent molecules as described in Section 2.2.2 in the Supporting Information.^{46,47,81} The degree of orbital coupling is affected by the different packing motifs and the relative orientation of the nearest neighbor molecules.

The computed charge transport parameters along different hopping dimers and charge carrier mobilities of the studied NFAs are listed in Table 4 and Table 5. In organic crystals, different molecular packing motifs along dissimilar hopping pathways and the variation in the charge transfer integrals of the central molecule with the adjacent molecules produces anisotropic mobility.^{82,83} The anisotropic mobility of the studied NFAs are evaluated using

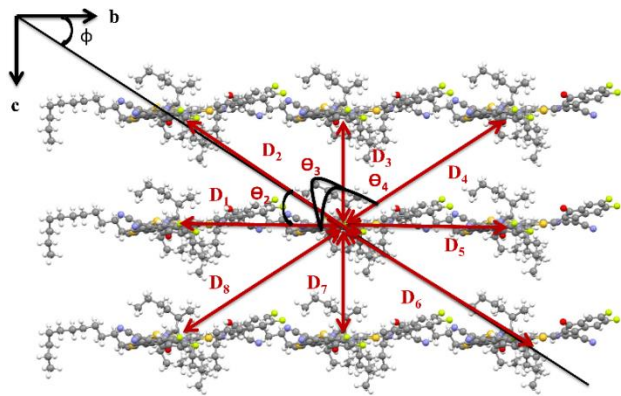
the formulation as described in Section S.2.4 in the Supporting information. The anisotropic electron/hole mobilities (μ_e/μ_h) of a subset of the studied NFAs are shown in Figure 7, while the plots for all other NFAs are available in Figure S10-S12 in the Supporting Information. The calculated mobilities are listed in Table 4 and Table 5. The maximum values of μ_e and μ_h in **AQx-2-c** are observed to be $5.47 \times 10^{-1} \text{ cm}^2\text{V}^{-1}\text{s}^{-1}$ and $4.15 \times 10^{-4} \text{ cm}^2\text{V}^{-1}\text{s}^{-1}$, respectively, corresponding to $\phi = 1.2^\circ/0.0^\circ$. Therefore, in **AQx-2-c**, the electron mobility is found to be much higher than the hole mobility suggesting its electron-transporting nature, and this observation is also supported by the higher electron transfer integrals (10.66 meV) and higher electron transfer rate ($1.4616 \times 10^{12} \text{ s}^{-1}$) along the same hopping channel. Among the designed NFAs, **AQx-2-ct3** exhibits the highest electron mobility of $6.03 \text{ cm}^2\text{V}^{-1}\text{s}^{-1}$, obtained along $\phi = 38.3^\circ/218.3^\circ$. All the designed NFAs have better charge carrier mobilities than the reference AQx-2. Hence, the designed NFAs may act as better electron transporting acceptor materials in organic photovoltaic applications. It is also observed that all the designed NFAs except **AQx-2-ct7** have better electron mobility than hole mobility, and hence, it suggests that our designed NFAs are promising electron transporting acceptor materials.

Table 4. The Intermolecular Distances (Measured Distance Between Their Mass-Centers) Along Different Pathways, Angle of Orientation (θ), Hole/Electron Couplings (V_h/V_e), Transfer Rates of Hole/Electron (K_h/K_e), and Angle-Resolved Hole/Electron Mobility Ranges (μ_h/μ_e) of the Designed NFAs

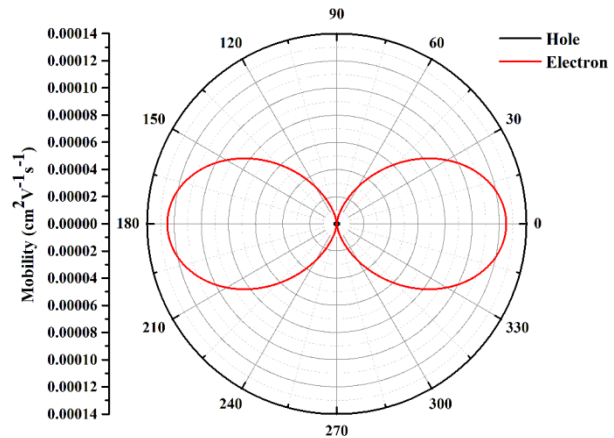
Comp.	Pathways	r (Å)	θ (deg)	V_h (meV)	V_e (meV)	K_h (s ⁻¹)	K_e (s ⁻¹)	μ_h (cm ⁻¹ V ⁻¹ s ⁻¹)	μ_e (cm ⁻¹ V ⁻¹ s ⁻¹)	μ_e/μ_h
AQx-2 (Ref.)	D1, D5	18.682	0	0.02	0.12	2.9116×10^6	1.8522×10^8	0- 1.97×10^{-6}	0- 1.25×10^{-4}	6.34×10^1
	D2, D6	22.628	34.35	0.00	0.00	0	0			
	D3, D7	12.767	90.00	0.00	0.00	0	0			
	D4, D8	22.628	145.65	0.00	0.00	0	0			
AQx-2-c	D1, D5	14.770	0	0.37	10.66	9.8410×10^8	1.4616×10^{12}	1.79×10^{-10} - 4.15×10^{-4}	9.83×10^{-3} - 5.47×10^{-1}	1.32×10^3
	D2, D6	19.795	42.20	0.01	4.16	7.1885×10^5	2.2259×10^{11}			
	D3, D7	13.296	90.45	0.00	0.01	0	1.2863×10^6			
	D4, D8	19.951	138.21	0.00	0.00	0	0			
AQx-2-ct1	D1, D5	15.033	0	0.69	4.23	3.5091×10^9	2.6370×10^{11}	1.34×10^{-7} - 1.52×10^{-3}	1.09×10^{-2} - 6.27×10^{-1}	4.12×10^2
	D2, D6	20.326	42.54	0.00	0.00	0	0			
	D3, D7	13.743	90.24	0.07	0.04	3.6116×10^7	2.3580×10^7			
	D4, D8	20.410	137.67	0.01	8.11	7.371×10^5	9.6934×10^{11}			
AQx-2-ct2	D1, D5	15.323	0	0.29	0.10	6.6007×10^8	1.6243×10^8	0- 3.00×10^{-4}	1.71×10^{-7} - 1.23×10^{-1}	4.10×10^2
	D2, D6	26.438	66.96	0.00	0.00	0	0			
	D3, D7	24.834	101.56	0.00	2.52	0	1.0315×10^{11}			
	D4, D8	31.687	129.84	0.00	0.01	0	1.6243×10^6			
AQx-2-ct3	D1, D5	16.207	0	0.07	0.14	3.944×10^7	3.6175×10^8	1.11×10^{-8} - 1.93×10^{-5}	2.94×10^{-6} -6.0262	3.12×10^5
	D2, D6	21.809	38.26	0.01	18.84	8.049×10^5	6.5512×10^{12}			
	D3, D7	13.537	86.12	0.01	0.01	8.049×10^5	1.8457×10^6			
	D4, D8	20.401	138.55	0.00	0.00	0	0			

Table 5. The Intermolecular Distances (Measured Distance Between Their Mass-Centers) Along Different Pathways, Angle of Orientation (θ), Hole/Electron Couplings (V_h/V_e), Transfer Rates of Hole/Electron (K_h/K_e), and Angle-Resolved Hole/Electron Mobility Ranges (μ_h/μ_e) of the

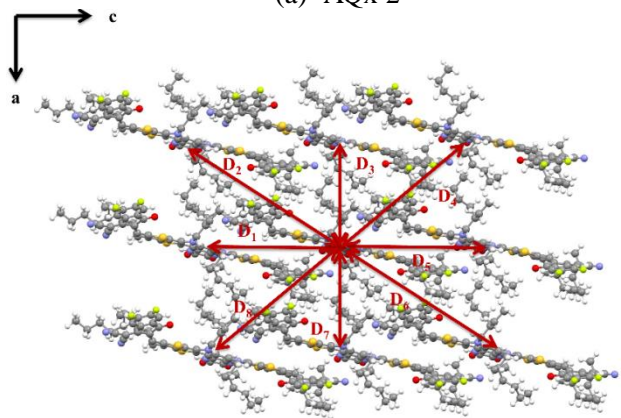
Comp.	Pathways	r (Å)	θ (deg)	V_h (meV)	V_e (meV)	K_h (s ⁻¹)	K_e (s ⁻¹)	μ_h (cm ⁻¹ V ⁻¹ s ⁻¹)	μ_e (cm ⁻¹ V ⁻¹ s ⁻¹)	μ_e/μ_h
AQx-2-ct4	D1, D5	13.208	0	0.79	2.33	5.0237×10^9	7.4718×10^{10}	6.17×10^{-5} - 3.04×10^{-2}	6.42×10^{-4} - 6.72×10^{-1}	2.20×10^1
	D2, D6	14.964	49.56	3.06	10.86	7.5372×10^{10}	1.6232×10^{12}			
	D3, D7	11.915	107.09	0.27	0.06	5.8681×10^8	4.9547×10^7			
	D4, D8	20.222	145.72	0.00	0.00	0	0			
AQx-2-ct5	D1, D5	19.211	0	0.03	3.28	6.0040×10^6	1.2942×10^{11}	3.54×10^{-7} - 3.87×10^{-5}	1.14×10^{-2} - 7.84×10^{-2}	2.03×10^3
	D2, D6	26.378	43.26	0.00	2.44	0	7.1620×10^{10}			
	D3, D7	18.076	90.00	0.10	0.89	6.6711×10^7	9.5287×10^9			
	D4, D8	26.378	136.74	0.00	0.00	0	0			
AQx-2-ct6	D1, D5	18.287	0	0.53	10.36	1.8973×10^9	6.0272×10^{11}	7.85×10^{-11} - 1.23×10^{-3}	0 - 3.89×10^{-1}	3.16×10^2
	D2, D6	18.490	44.64	0.01	0.00	6.7544×10^5	0			
	D3, D7	13.967	111.55	0.00	0.00	0	0			
	D4, D8	26.779	150.98	0.00	0.00	0	0			
AQx-2-ct7	D1, D5	20.071	0	3.47	2.24	9.2155×10^{10}	2.5877×10^{10}	3.64×10^{-3} - 8.71×10^{-1}	1.732×10^{-3} - 1.212×10^{-1}	1.39×10^{-1}
	D2, D6	25.108	44.44	10.19	4.81	7.9470×10^{11}	1.1932×10^{11}			
	D3, D7	17.710	96.95	0.45	0.19	1.5498×10^9	1.8617×10^8			
	D4, D8	28.329	141.64	0.00	0	0	0			
AQx-2-ct8	D1, D5	13.453	0	0.09	0.02	6.6873×10^7	3.1395×10^6	8.85×10^{-6} - 1.27×10^{-5}	1.52×10^{-9} - 5.05×10^{-4}	3.97×10^1
	D2, D6	17.917	34.84	0.00	0.00	0	0			
	D3, D7	10.313	83.03	0.11	0.56	9.9897×10^7	2.4613×10^9			
	D4, D8	15.927	140.00	0.01	0.00	8.2559×10^5	0			



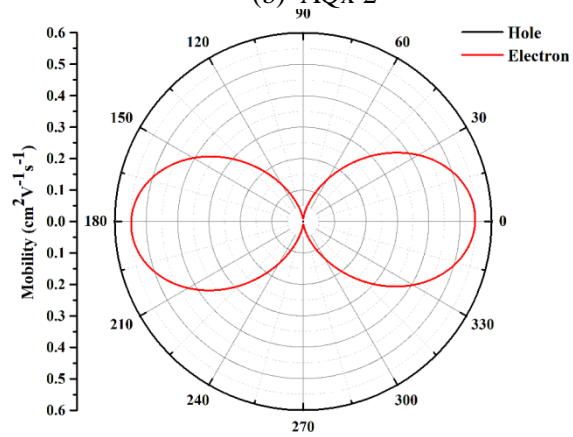
(a) AQx-2



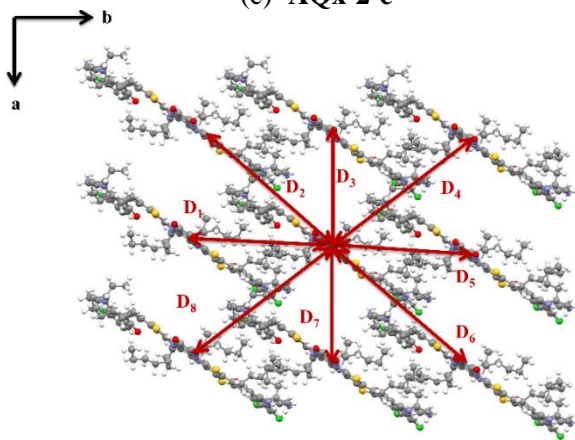
(b) AQx-2



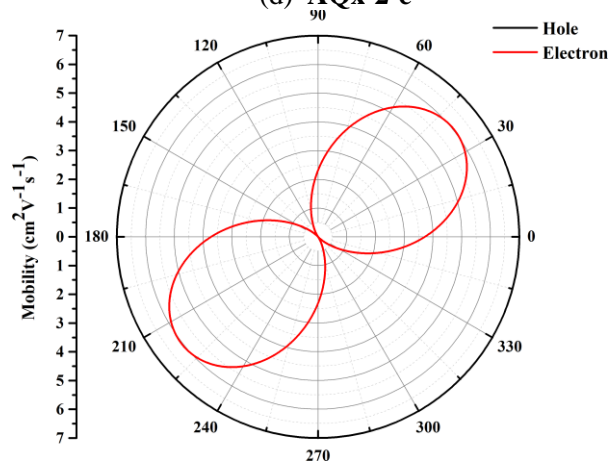
(c) AQx-2-c



(d) AQx-2-c



(e) AQx-2-ct3



(f) AQx-2-ct3

Figure 7: Simulated crystal structures showing different hopping channels and angle resolved mobility of the studied NFAs (AQx-2, AQx-2-c, AQx-2-ct3).

Absorption Properties and Charge Transfer Analysis of the D/A Blends.

The optical absorption of D/A blends and the charge transfer mechanism from donor to acceptor play important roles in the organic photovoltaic performance. The blends of the PM6 donor and designed NFAs are built by A-A stacking. The A-A stacking of such D/A blends was widely accepted because such a stacking pattern seems to be dominant and favorable for exciton dissociation and charge transfer.^{2,84} In the complex systems of the designed NFAs and the PM6 donor, A-A stacking involves the terminal electron-withdrawing end groups of the NFAs and the electron-withdrawing unit of the polymer donor. To simplify the calculations, in our study, only one repeat unit of the polymer donor PM6 was taken into account, and unsaturated atoms were hydrogenated. Initially, the distance between the terminal electron-withdrawing end groups of the NFAs and the electron-withdrawing unit of the PM6 has been set as 3.5 Å (Figure 8). Further, we optimized the D/A (PM6:NFA) blend structure using the cost-effective extended tight-binding (GFN2-xTB) method.⁵¹ To analyze the optical properties and charge transfer behaviour of the PM6:NFA blends, TD-DFT calculations are carried out at the CAM-B3LYP/6-31G(d,p) level of theory in the solvent (Chloroform) phase based on GFN2-xTB optimized geometries. It is observed from Table 6 and Figure 9 that the maximum absorption wavelengths (503-610 nm) of the PM6:NFA blends lie in the visible region of the solar spectrum. The light harvesting efficiencies (η_s) of the blends are computed corresponding to the brightest excited state transition. The computed light harvesting efficiencies lie in the range of 0.9589-0.9957, which indicates efficient light harvesting by the PM6:NFA blends during solar cell device operation. Among the designed blends, PM6:AQx-2-ct6 and PM6:AQx-2-ct8 have slightly smaller light harvesting efficiencies compared to the other blends and, therefore, the other PM6:NFA blends may have better short-circuit current density values. The intermolecular charge transfer (CT) states of the PM6:NFA blends are identified by natural transition orbital (NTO) analysis considering the first 40 excited states, as shown for AQx-2, AQx-2-c and AQx-2-ct3 in Figure 10 and all the other NFAs are given in Figures S13-S14 in the Supporting Information. In the CT state, the HOMO predominantly localizes on the donor PM6 and the LUMO localizes on the acceptor NFA. The excited state properties of the corresponding CT states, along with NTO contributions, are listed in Table S8 in the Supporting Information. In addition, the Δr parameter is also evaluated for the listed excited states to verify their CT nature (Table S8). The computed values of the Δr parameter are found to be larger than 2.0 Å (6.2-15.4 Å), which indicates that the identified excited states are mainly charge transfer (CT) states.^{54,85} We also carried out interfragment charge transfer (IFCT) analysis to validate the nature of the excitation and to quantify the net electron transfer from the donor PM6 fragment to acceptor fragments. The contribution of each fragment to the hole and electron as well as the percentage of transferred electrons between the donor and acceptor fragments are listed in Table 7. The percentage of intrafragment charge transfer is improved for the designed PM6:NFA blends (except PM6:AQx-2-ct5) compared to the PM6:AQx-2 (reference NFA) blend. Thus, for those designed PM6:NFA blends, the interfacial exciton dissociation process may be easier than the previously reported

PM6 and AQx-2 blend and the newly designed PM6:NFA blends may promote better charge carrier separation at the D/A interface.

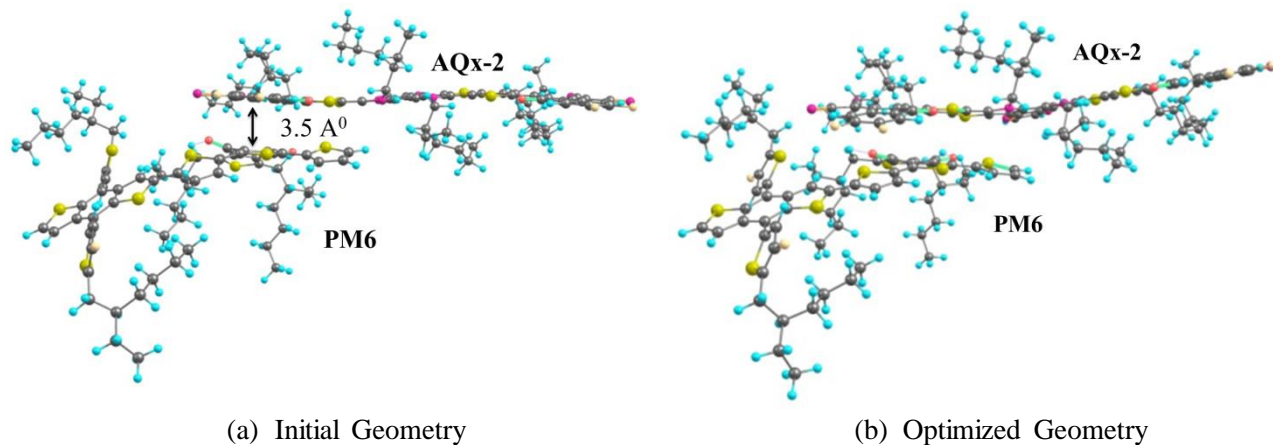


Figure 8. The initial and optimized geometries of the investigated PM6/NFAs blends (Representative blend: PM6:AQx-2).

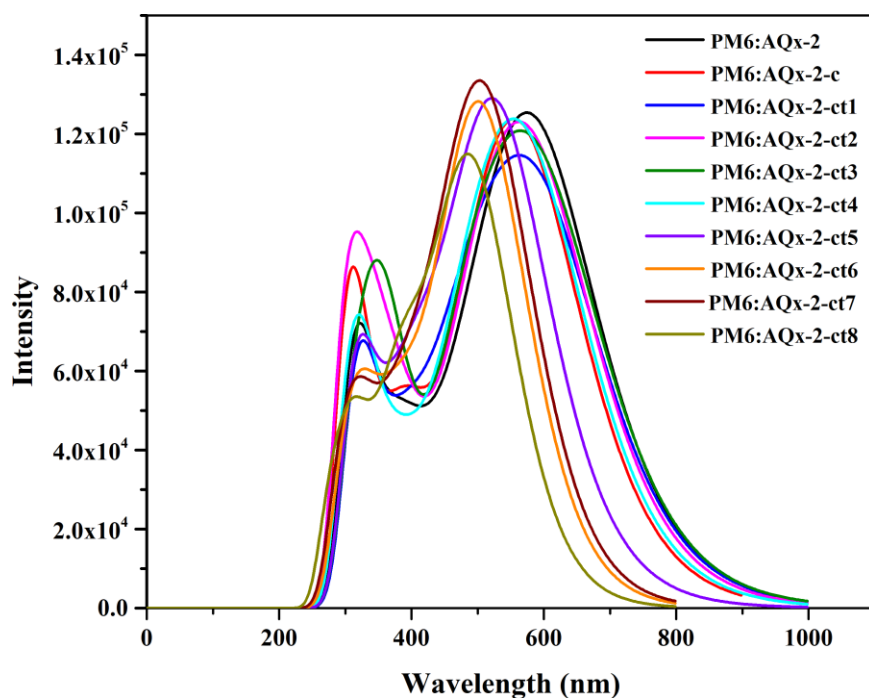


Figure 9: The optical absorption spectra of the investigated PM6/NFAs complexes at the CAM-B3LYP/6-31G(d,p) level of theory in the solvent (Chloroform) phase. Spectra include the lowest 40 excitations with Gaussian lineshape with peak half-width at half height: 0.333 eV.

Table 6. Computed Electronic Transition Energy E (eV), Absorption Wavelength λ_{abs} (nm), Major Configurations, Oscillator Strength (f), and Light Harvesting Efficiency (η_{λ}) of the PM6/NFA Blends as Determined at the CAM-B3LYP/6-31G(d,p) Level of Theory in the Solvent (Chloroform) Phase

Complex	State	E (eV)	λ_{abs} (nm)	major config.	f	η_{λ}
PM6:AQx-2	$S_0 \rightarrow S_1$	2.05	604	H-1 \rightarrow L (56%)	2.3215	0.9952
	$S_0 \rightarrow S_3$	2.51	495	H-1 \rightarrow L+1 (51%)	0.6992	
PM6:AQx-2-c	$S_0 \rightarrow S_1$	2.11	588	H-1 \rightarrow L (75%)	2.2281	0.9941
	$S_0 \rightarrow S_3$	2.46	503	H \rightarrow L+2 (37%)	0.7841	
PM6:AQx-2-ct1	$S_0 \rightarrow S_1$	2.03	609	H-1 \rightarrow L (49%)	2.0369	0.9908
	$S_0 \rightarrow S_4$	2.55	486	H \rightarrow L+3 (42%)	0.9240	
PM6:AQx-2-ct2	$S_0 \rightarrow S_1$	2.06	601	H-1 \rightarrow L (75%)	2.2259	0.9941
	$S_0 \rightarrow S_3$	2.45	507	H-1 \rightarrow L+1 (44%)	0.7357	
PM6:AQx-2-ct3	$S_0 \rightarrow S_1$	2.03	610	H-1 \rightarrow L (73%)	2.1759	0.9933
	$S_0 \rightarrow S_4$	2.54	488	H \rightarrow L+2 (54%)	0.9148	
PM6:AQx-2-ct4	$S_0 \rightarrow S_1$	2.09	593	H-1 \rightarrow L (50%)	2.2159	0.9939
	$S_0 \rightarrow S_4$	2.55	485	H \rightarrow L+2 (36%)	0.9035	
PM6:AQx-2-ct5	$S_0 \rightarrow S_1$	2.06	602	H \rightarrow L (61%)	0.2734	
	$S_0 \rightarrow S_2$	2.30	538	H-1 \rightarrow L (42%)	2.3658	0.9957
	$S_0 \rightarrow S_4$	2.60	478	H \rightarrow L+3 (38%)	0.6087	
PM6:AQx-2-ct6	$S_0 \rightarrow S_1$	2.37	523	H \rightarrow L (75%)	1.6703	0.9786
	$S_0 \rightarrow S_2$	2.47	503	H-1 \rightarrow L+1 (66%)	1.0402	
PM6:AQx-2-ct7	$S_0 \rightarrow S_1$	2.35	528	H-1 \rightarrow L (61%)	2.1199	0.9924
	$S_0 \rightarrow S_3$	2.71	457	H-1 \rightarrow L+1 (34%)	1.0586	
PM6:AQx-2-ct8	$S_0 \rightarrow S_1$	2.46	503	H \rightarrow L+2 (34%)	1.3863	0.9589
	$S_0 \rightarrow S_2$	2.54	488	H-1 \rightarrow L (80%)	1.1781	

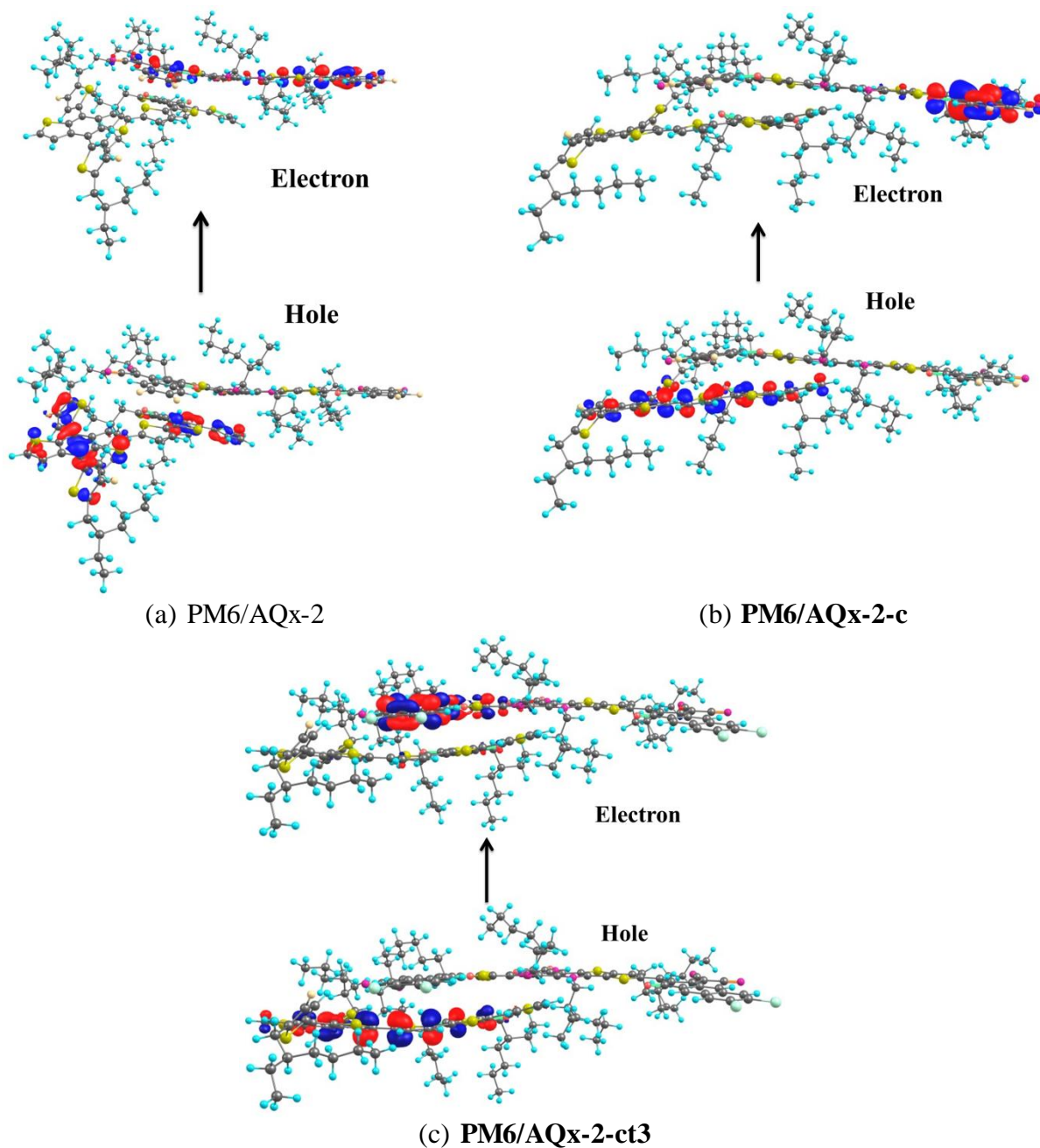


Figure 10: The NTO analysis of the CT excited states of the investigated PM6/NFA (AQx-2, AQx-2-c, AQx-2-ct3) blends. The blue and red colors represent the positive and negative isosurfaces, respectively.

Table 7. Contribution of Donor, Acceptor Fragments to Hole and Electron and Percentage of Interfragment Charge Transfer (IFCT) Between Donor, Acceptor Fragments in CT States

Complex	CT state	Hole (Electron)	Hole (Electron)	IFCT (PM6 → NFA)	IFCT (NFA → PM6)
		contribution of PM6	contribution of NFAs		
PM6:AQx-2	S28	71.54% (5.27%)	28.46% (94.73%)	67.76%	1.50%
PM6:AQx-2-c	S38	96.64% (0.97%)	3.36% (99.03%)	95.70%	0.03%
PM6:AQx-2-ct1	S30	92.61% (22.76%)	7.39% (77.24%)	71.53%	1.68%
PM6:AQx-2-ct2	S29	90.08% (8.30%)	9.92% (91.70%)	82.60%	0.82%
PM6:AQx-2-ct3	S33	91.84% (24.88%)	8.16% (75.12%)	68.99%	2.03%
PM6:AQx-2-ct4	S30	86.91% (9.90%)	13.09% (90.10%)	78.30%	1.29%
PM6:AQx-2-ct5	S38	69.53% (12.33%)	30.47% (87.67%)	60.95%	3.76%
PM6:AQx-2-ct6	S23	77.70% (2.98%)	22.30% (97.02%)	75.39%	0.66%
PM6:AQx-2-ct7	S19	91.70% (4.85%)	8.30% (95.15%)	87.25%	0.40%
PM6:AQx-2-ct8	S30	99.62 % (15.10%)	0.38 % (84.90%)	84.58%	0.06%

CONCLUSION

In the present study, we theoretically designed a series of non-fullerene acceptors (NFAs) based on the previously reported crescent shaped AQx-2. At first, we performed core modulation of the reported AQx-2 and designed a new NFA, namely **AQx-2-c**, in which the quinoxaline core of AQx-2 is replaced by 2,3-quinoxalinedione,1,4-dihydro having a weaker electron donating ability than quinoxaline. Further, we designed a series of eight more NFAs by performing terminal-unit engineering of **AQx-2-c** (terminal unit: Fluorinated IC) with various halogen substituted, π -extended, thienyl fused IC groups and different end-capped groups other than IC also. We explored the geometrical, optoelectronic, intra and intermolecular charge transport properties, and overall photovoltaic performance of the designed crescent shaped NFAs with respect to the PM6 donor. From the geometrical analysis, we observed that all the designed NFAs except **AQx-2-ct8** have near planar conjugated backbones as their dihedral angles do not vary significantly from zero. All the computed C-C bond lengths exhibited significant double bond character, which facilitates the delocalization of π -electrons over the whole molecular backbone and improves the charge transport properties. From frontier molecular orbital analysis, the computed HOMO levels of the investigated designed NFAs were below the air oxidation threshold (ca. -5.27 eV or 0.57 V vs saturated calomel electrode (SCE)) and found to be air-stable. Except for **AQx-2-ct6**, all the designed NFAs could have more n-type character as their computed LUMO levels were found to be close to -4.0 eV and their adiabatic electron affinity values were observed to be higher than 2.4 eV. This observation was also supported by the

significantly lower electron injection barriers of the studied NFAs other than for **AQx-2-ct6**. The designed NFAs except for **AQx-2-ct5**, **AQx-2-ct6**, and **AQx-2-ct7** may favor better electron injection than the reported AQx-2 as they had smaller electron injection barriers due to their lower-lying LUMO levels. The studied NFAs could act as potential non-fullerene acceptor candidates as they were found to have sufficient open-circuit voltages and fill factors ranging from 0.62-1.41 eV and 83%-91%, respectively. All the newly designed NFAs except **AQx-2-ct5**, **AQx-2-ct6**, and **AQx-2-ct7**, were expected to have larger electron withdrawing abilities than the reported AQx-2 as they have higher Mulliken electronegativity indices than AQx-2. From the anisotropic mobility analysis, it was noted that all the designed NFAs have better charge carrier mobilities than the reference AQx-2. It was also found that all the designed NFAs except **AQx-2-ct7** had better electron mobilities than hole mobilities, and hence, it suggests that our designed NFAs could perform as good electron transport acceptor materials in organic solar cells. The charge density difference (CDD) analysis suggested that the structural modulation of the core and terminal units had only a small impact on intramolecular charge transfer amounts (q_{CT}) as the computed values of q_{CT} for the reference AQx-2 and the studied NFAs did not change significantly (0.63-0.67 |e⁻|). However, **AQx-2-ct2** and **AQx-2-ct3**, having longer π -conjugated terminal units, showed relatively longer D_{CT} than the other NFAs, suggesting more difficult intramolecular charge recombination and easier charge transfer for these two compounds. The excitations found in the TDM map were delocalized over the whole molecular backbone, and during the excitation process, the electrons were found to be slightly migrated from the D to the terminal acceptor (A_2) part. From the optical absorption analysis, all the designed NFAs had the maximum absorption spectra ranging from 597 nm-730 nm, which lay in the visible and near infra-red (IR) regions of the solar spectrum. Among the studied NFAs, the absorption profile of **AQx-2-ct3** showed the maximum red-shift (730 nm) due to its extended π -conjugated terminal unit containing the electron withdrawing -Cl atoms. The computed light harvesting efficiencies for **AQx-2-c**, **AQx-2-ct1**, **AQx-2-ct2**, **AQx-2-ct3**, and **AQx-2-ct4** were found to be slightly higher than the other designed NFAs and they may exhibit better short-circuit current density. The simulated maximum absorption wavelengths (503-610 nm) of the PM6:NFA blends were observed to lie in the visible region of the solar spectrum. The computed light harvesting efficiencies for the D/A blends were found to be in the range of 0.9589-0.9957, which indicates efficient light harvesting by the PM6:NFA blends during solar cell device operation. Among the designed blends, PM6:**AQx-2-ct6** and PM6:**AQx-2-ct8** have slightly smaller light harvesting efficiencies compared to the other blends, and therefore, the other PM6:NFA blends may have better short-circuit current density values. From the intrafragment charge transfer (IFCT) analysis, it was observed that the amount of intrafragment charge transfer is improved for the designed PM6:NFA blends (except PM6:**AQx-2-ct5**) over the PM6:AQx-2 (reference NFA) blend. The fact indicates that, for our designed PM6:NFA blends, the interfacial exciton dissociation process may be easier than the previously reported PM6:AQx-2 blend, and the newly designed PM6:NFA blends may promote better charge carrier separation at the D/A interface. It is also noted that among all the newly designed NFAs, **AQx-2-ct3** may be the best

choice as an acceptor material. **AQx-2-ct3** had the lowest optical band gap (1.70 eV) along with the maximum red-shifted optical absorption (730 nm) as it had an extended π -conjugated terminal unit containing the electron withdrawing -Cl atoms. The lowest electron injection barrier and lowest electron reorganization energy led to the highest electron mobility $6.03 \text{ cm}^2 \text{V}^{-1} \text{s}^{-1}$ of **AQx-2-ct3**. In addition, **AQx-2-ct3** had better ICT properties than other designed NFAs as it had the highest D_{CT} and $\Delta\mu_{CT}$.

In summary, our theoretical investigation showed a series of promising non-fullerene acceptors, and we expect that our study will provide further insight into the theoretical basis for the synthesis of high performance $A_2\text{-}D A_1 D\text{-}A_2$ type NFAs in organic photovoltaic applications. Moreover, it can be concluded that structural modulation of the core and the terminal units can be an effective strategy to tune the optoelectronic, charge transport, and overall photovoltaic properties of the non-fullerene acceptor molecules.

Acknowledgement

The research was enabled with computational resources provided by the Indian Institute of Technology (Indian School of Mines), Dhanbad and Compute/Calcul Canada (computeCanada.ca). L. Bhattacharya and S. Sahu is thankful to Indian Institute of Technology (Indian School of Mines), Dhanbad for research support. L. Bhattacharya is grateful to the Science and Engineering Board (SERB) India and University of Alberta, Canada for SERB-University of Alberta Overseas Visiting Doctoral Fellowship. L. Bhattacharya is also thankful to R. Khatua and S. Debata for discussions on crystal structure prediction and anisotropic mobility calculations.

Supporting Information Available

The supporting information contains crystal structure prediction details, theory related to charge transfer integral, charge transfer rate and anisotropic mobility, Table S1-S8, and Figure S1-S14.

References

- (1) Saleem, R; Farhat, A.; Khera, R. A.; Langer, P.; Iqbal J. Designing of small molecule non-fullerene acceptors with cyanobenzene core for photovoltaic application. *Comp. Theor. Chem.* **2021**, *1197*, 113154.
- (2) Yang, J; Li, Q. -S; Li, Z. -S. Theoretical design of asymmetric $AD_1 - A'D_2 - A$ type non-fullerene acceptors for organic solar cells. *Phys. Chem. Chem. Phys.* **2021**, *23*, 12321-12328.
- (3) Lin, F; Jiang, K; Kaminsky, W; Zhu, Z; Jen, A. K. -Y. A non-fullerene acceptor with enhanced intermolecular π -core interaction for high-performance organic solar cells. *J. Am. Chem. Soc.* **2020**, *142*, 15246-15251.

- (4) Mahmood, A.; Tang, A.; Wang, X.; Zhou, E. First-principles theoretical designing of planar non-fullerene small molecular acceptors for organic solar cells: manipulation of noncovalent interactions. *Phys. Chem. Chem. Phys.* **2019**, *21*, 2128-2139.
- (5) Liu, J.; Li, J.; Liu, X.; Li, F.; Tu, G. Amphiphilic diblock fullerene derivatives as cathode interfacial layers for organic solar cells. *ACS Appl. Mater. Interfaces* **2018**, *10*, 2649-2657.
- (6) Li, M.-Y.; Yin, H.; Sui, M.-Y.; Wang, F.; Liu, Y.-H.; Sun, G.-Y. In-depth probe of researching interfacial charge transfer process for organic solar cells: A promising bisadduct fullerene derivatives acceptor. *Int J Quantum Chem.* **2019**, *119*, e25938.
- (7) He, Y.; Li, Y. Fullerene derivative acceptors for high performance polymer solar cells. *Phys. Chem. Chem. Phys.* **2011**, *13*, 1970-1983.
- (8) Kuznetsov, I. E.; Susarova, D. K.; Inasaridze, L. N.; Klyuev, M. V.; Troshin, P. A. Synthesis of statistical carbazole-fluorene-thiophene-benzothiadiazole copolymers and their investigation in organic solar cells. *Mendeleev. Commun.* **2015**, *25*, 277-279.
- (9) Holliday, S.; Ashraf, R. S.; Wadsworth, A.; Baran, D.; Amber Yousaf, S.; Nielsen, C. B.; Tan, C.-H.; Dimitrov, S. D.; Shang, Z.; Gasparini, N.; Alamoudi, M.; Laquai, F.; Brabec, C. J.; Salleo, A.; Durrant, J. R.; McCulloch, I. High-efficiency and air-stable P3HT-based polymer solar cells with a new non-fullerene acceptor. *Nat. Comm.* **2016**, *7*, 11585.
- (10) Zhao, F.; Dai, S.; Wu, Y.; Zhang, Q.; Wang, J.; Jiang, L.; Ling, Q.; Wei, Z.; Ma, W.; You, W.; Wang, C.; Zhan, X. Single-junction binary-blend nonfullerene polymer solar cells with 12.1% efficiency. *Adv. Mater.* **2017**, *29*, 1700144.
- (11) Lin, Y.; Zhang, Z.-G.; Bai, H.; Wang, J.; Yao, Y.; Li, Y.; Zhua, D.; Zhan, X. High-performance fullerene-free polymer solar cells with 6.31% efficiency. *Energy Environ. Sci.* **2015**, *8*, 610-616.
- (12) Jia, B.; Wang, J.; Wu, Y.; Zhang, M.; Jiang, Y.; Tang, Z.; Russell, T. P.; Zhan, X. Enhancing the performance of a fused-ring electron acceptor by unidirectional extension. *J. Am. Chem. Soc.* **2019**, *141*, 19023-19031.
- (13) Yue, Q.; Liu, W.; Zhu, X. n-Type molecular photovoltaic materials: design strategies and device applications. *J. Am. Chem. Soc.* **2020**, *142*, 11613-11628.
- (14) Zhang, G.; Zhao, J.; Chow, P. C. Y.; Jiang, K.; Zhang, J.; Zhu, Z.; Zhang, J.; Huang, F.; Yan, H. Nonfullerene acceptor molecules for bulk heterojunction organic solar cells. *Chem. Rev.* **2018**, *118*, 3447-3507.
- (15) Yan, C.; Barlow, S.; Wang, Z.; Yan, H.; Jen, A. K.-Y.; Marder S. R.; Zhan, X. Nonfullerene acceptors for organic solar cells. *Nat. Rev. Mater.* **2018**, *3*, 18003.
- (16) Suman; Singh, S. P. Impact of end groups on the performance of non-fullerene acceptors for organic solar cell applications. *J. Mater. Chem. A* **2019**, *7*, 22701-22729.
- (17) Ahmed, S.; Kalita, D. J. End-capped group manipulation of non-fullerene acceptors for efficient organic photovoltaic solar cells: a DFT study. *Phys. Chem. Chem. Phys.* **2020**, *22*, 23586-23596.

- (18) Yi, Y. -Q. -Q.; Feng, H.; Chang, M.; Zhang, H.; Wan, X.; Li, C.; Chen, Y. New small-molecule acceptors based on hexacyclic naphthalene (cyclopentadithiophene) for efficient non-fullerene organic solar cells. *J. Mater. Chem. A* **2017**, *5*, 17204-17210.
- (19) Ma, Y.; Zhang, M.; Yan, Y.; Xin, J.; Wang, T.; Ma, W.; Tang, C.; Zheng, Q. Ladder type dithienonaphthalene-based small-molecule acceptors for efficient nonfullerene organic solar cells. *Chem. Mater.* **2017**, *29*, 7942-7952.
- (20) Wang, W.; Yan, C.; Lau, T. -K.; Wang, J.; Liu, K.; Fan, Y.; Lu, X.; Zhan, X. Fused hexacyclic nonfullerene acceptor with strong near-infrared absorption for semitransparent organic solar cells with 9.77% efficiency. *Adv. Mater.* **2017**, *29*, 1701308.
- (21) Shi, X.; Zuo, L.; Jo, S. B.; Gao, K.; Lin, F.; Liu, F.; Jen, A. K. -Y. Design of a highly crystalline low-band gap fused-ring electron acceptor for high-efficiency solar cells with low energy loss. *Chem. Mater.* **2017**, *29*, 8369-8376.
- (22) Lin, Y.; Wang, J.; Zhang, Z. -G.; Bai, H.; Li, Y.; Zhu, D.; Zhan, X. An electron acceptor challenging fullerenes for efficient polymer solar cells. *Adv. Mater.* **2015**, *27*, 1170-1174.
- (23) Zhao, W.; Li, S.; Yao, H.; Zhang, S.; Zhang, Y.; Yang, B.; Hou, J. Molecular optimization enables over 13% efficiency in organic solar cells. *J. Am. Chem. Soc.* **2017**, *139*, 7148-7151.
- (24) Feng, L.; Yuan, J.; Zhang, Z.; Peng, H.; Zhang, Z. -G.; Xu, S.; Liu, Y.; Li, Y.; Zou, Y. Thieno[3,2-*b*]pyrrolo-Fused Pentacyclic Benzotriazole-Based Acceptor for Efficient Organic Photovoltaics. *ACS Appl. Mater. Interfaces* **2017**, *9*, 31985-31992.
- (25) Yang, Y. The original design principles of the Y-series nonfullerene acceptors, from Y1 to Y6. *ACS Nano* **2021**, *15*, 18679-18682.
- (26) Liu, Q.; Jiang, Y.; Jin, K.; Qin, J.; Xu, J.; Li, W.; Xiong, J.; Liu, J.; Xiao, Z.; Sun, K.; Yang, S.; Zhang, X.; Ding, L. 18% Efficiency organic solar cells. *Sci. Bull.* **2020**, *65*, 272-275.
- (27) Khan, M. U.; Hussain, R.; Mehboob, M. Y.; Khalid, M.; Shaq, Z.; Aslam, M.; Al- Saadi, A. A.; Jamil, S.; Janjua, M. R. S. A. In silico modeling of new Y-Series-based near-infrared sensitive non-fullerene acceptors for efficient organic solar cells. *ACS Omega* **2020**, *5*, 24125-24137.
- (28) Yang, J.; Ding, W. -L.; Li, Q. -S.; Li, Z. -S. Theoretical Study of Non-Fullerene Acceptors Using End-Capped Groups with Different Electron-Withdrawing Abilities toward Efficient Organic Solar Cells. *J. Phys. Chem. Lett.* **2022**, *13*, 916-922.
- (29) Zhou, Z.; Liu, W.; Zhou, G.; Zhang, M.; Qian, D.; Zhang, J.; Chen, S.; Xu, S.; Yang, C.; Gao, F.; Zhu, H.; Liu, F.; Zhu, X. Subtle molecular tailoring induces significant morphology optimization enabling over 16% efficiency organic solar cells with efficient charge generation. *Adv. Mater.* **2020**, *32*, 1906324.
- (30) Huang, J.; Tang, H.; Yan, C.; Li, G. 1, 1-Dicyanomethylene-3-indanone end-cap engineering for fused-ring electron acceptor-based high-performance organic photovoltaics. *Cell Rep. Phys. Sci.* **2021**, *2*, 100292.

- (31) Liu, X.; Shen, W.; He, R.; Luo, Y.; Li, M. Strategy to modulate the electron-rich units in donor-acceptor copolymers for improvements of organic photovoltaics. *J. Phys. Chem. C* **2014**, *118*, 17266-17278.
- (32) Khlaifa, D.; Massuyeau, F.; Ewels, C. P.; Duvail, J. -L.; Faulques, E.; Alimi, K. DFT Modeling of Novel Donor-Acceptor (D-A) Molecules Incorporating 3-hexylthiophene (3HT) for Bulk Heterojunction Solar Cells. *ChemistrySelect* **2017**, *2*, 10082-10090.
- (33) Becke, D. Density-functional thermochemistry. III. The role of exact exchange. *J. Chem. Phys.* **1993**, *98*, 5648-5652.
- (34) Grimme, S.; Ehrlich, S.; Goerigk, L. Effect of the damping function in dispersion corrected density functional theory. *J. Comp. Chem.* **2011**, *32*, 1456-1465.
- (35) Perdew, J. P.; Burke, K.; Ernzerhof, M. Generalized Gradient Approximation Made Simple. *Phys. Rev. Lett.* **1996**, *77*, 3865-3868.
- (36) Adamo, C.; Barone, V. Exchange functionals with improved long-range behavior and adiabatic connection methods without adjustable parameters: The mPW and mPW1PW models. *J. Chem. Phys.* **1998**, *108*, 664-675.
- (37) Zhao, Y.; Truhlar, D. G. The M06 suite of density functionals for main group thermochemistry, thermochemical kinetics, noncovalent interactions, excited states, and transition elements: two new functionals and systematic testing of four M06-class functionals and 12 other functionals. *Theor. Chem. Acc.* **2008**, *120*, 215241.
- (38) Chai, J.-D.; Head-Gordon, M. Long-range corrected hybrid density functionals with damped atom-atom dispersion corrections. *Phys. Chem. Chem. Phys.* **2008**, *10*, 6615- 6620.
- (39) Cui, Y.; Yao, H.; Zhang, J.; Zhang, T.; Wang, Y.; Hong, L.; Xian, K.; Xu, B.; Zhang, S.; Peng, J.; Wei, Z.; Gao, F.; Hou, J. Over 16% efficiency organic photovoltaic cells enabled by a chlorinated acceptor with increased open-circuit voltages. *Nat. Comm.* **2019**, *10*, 2515.
- (40) Zou, X.; Wen, G.; Hu, R.; Dong, G.; Zhang, C.; Zhang, W.; Huang, H.; Dang, W. An Insight into the Excitation States of Small Molecular Semiconductor Y6. *Molecules* **2020**, *25*, 4118.
- (41) BIOVIA, D. S., Materials Studio 2017. Dassault Systèmes, San Diego Google Scholar **2017**.
- (42) Mighell, A. D.; Ondik, H. M.; Molino., B. B. Crystal data space-group tables. *J. Phys. Chem. Ref. Data* **1977**, *6*, 675.
- (43) Debata, S.; Sahoo, S. R.; Khatua, R.; Sahu, S. Rational design and crystal structure prediction of ring-fused double-PDI compounds as n-channel organic semiconductors: a DFT study. *Phys. Chem. Chem. Phys.* **2021**, *23*, 12329-12339.
- (44) Khatua, R.; Debata, S.; Sahu, S. Computational study of electron transport in halogen incorporated diindenotetracene compounds: crystal structure, charge transport and optoelectronic properties. *Phys. Chem. Chem. Phys.* **2022**, Advance Article, <https://doi.org/10.1039/D1CP05784G>.

- (45) Debata, S.; Khatua, R.; Sahu, S. Synergistic effects of side-functionalization and aza-substitution on the charge transport and optical properties of perylenebased organic materials: a DFT study. *New J. Chem.* **2022**, Advance Article, <https://doi.org/10.1039/D1NJ06084H>.
- (46) ADF 2019.3, SCM, Theoretical Chemistry, Vrije Universiteit, Amsterdam, The Netherlands, <http://www.scm.com>, Optionally, you may add the following list of authors and contributors: Baerends, E. J.; Ziegler, T.; Atkins, A. J.; Autschbach, J.; Baseggio, O.; Bashford, D.; Bérces, A.; Bickelhaupt, F. M.; Bo, C.; Boerrigter, P. M.; Cavallo, L.; Daul, C.; Chong, D. P.; Chulhai, D. V.; Deng, L.; Dickson, R. M.; Dieterich, J. M.; Ellis, D. E.; van Faassen, M.; Fan, L.; Fischer, T. H.; Förster, A.; Fonseca Guerra, C.; Franchini, M.; Ghysels, A.; Giammona, A.; van Gisbergen, S. J. A.; Goetz, A.; Götz, A. W.; Groeneveld, J. A.; Gritsenko, O. V.; Grüning, M.; Gusarov, S.; Harris, F. E.; van den Hoek, P.; Hu, Z.; Jacob, C. R.; Jacobsen, H.; Jensen, L.; Joubert, L.; Kaminski, J. W.; van Kessel, G.; König, C.; Kootstra, F.; Kovalenko, A.; Krykunov, M. V.; van Lenthe, E.; McCormack, D. A.; Michalak, A.; Mitoraj, M.; Morton, S. M.; Neugebauer, J.; Nicu, V. P.; Noodleman, L.; Osinga, V. P.; Patchkovskii, S.; Pavanello, M.; Peeples, C. A.; Philipsen, P. H. T.; Post, D.; Pye, C. C.; Ramanantoanina, H.; Ramos, P.; Ravenek, W.; Rodríguez, J. I.; Ros, P.; Rüger, R.; Schipper, P. R. T.; Schlüns, D.; van Schoot, H.; Schreckenbach, G.; Seldenthuis, J. S.; Seth, M.; Snijders, J. G.; Solà, M.; Stener, M.; Swart, M.; Swerhone, D.; Tognetti, V.; te Velde, G.; Vernooijs, P.; Versluis, L.; Visscher, L.; Visser, O.; Wang, F.; Wesolowski, T. A.; Wesolowski, E. M.; Wiesenekker, G.; Wol, S. K.; Woo, T. K.; Yakovlev, A. L.
- (47) Senthilkumar, K.; Grozema, F. C.; Bickelhaupt, F. M.; Siebbeles, L. D. A. Charge transport in columnar stacked triphenylenes: Effects of conformational fluctuations on charge transfer integrals and site energies. *J. Chem. Phys.* **2003**, *119*, 9809-9817.
- (48) Liu, L.; Yang, G.; Duan, Y.; Geng, Y.; Wu, Y.; Su, Z. The relationship between intermolecular interactions and charge transport properties of triuoromethylated polycyclic aromatic hydrocarbons. *Org. Electron.* **2014**, *15*, 1896-1905.
- (49) Delgado, M. C. R.; Kim, E. -G.; da Silva Filho, D. A.; Bredas, J. -L. Tuning the charge-transport parameters of perylene diimide single crystals via end and/or core functionalization: a density functional theory investigation. *J. Am. Chem. Soc.* **2010**, *132*, 3375-3387.
- (50) Duan, Y. -A.; Li, H. -B.; Geng, Y.; Wu, Y.; Wang, G. -Y.; Su, Z. -M. Theoretical studies on the hole transport property of tetrathienoarene derivatives: The influence of the position of sulfur atom, substituent and p-conjugated core. *Org. Electron.* **2014**, *15*, 602-613.
- (51) Bannwarth, C.; Ehlert, S.; Grimme, S. GFN2-xTB-An Accurate and Broadly Parametrized Self-Consistent Tight-Binding Quantum Chemical Method with Multipole Electrostatics and Density-Dependent Dispersion Contributions. *J. Chem. Theory Comput.* **2019**, *15*, 1652-1671.
- (52) Wang, Q.; Li, Y.; Song, P.; Su, R.; Ma, F.; Yang, Y. Non-fullerene acceptor-based solar cells: From structural design to interface charge separation and charge transport. *Polymers* **2017**, *9*, 692.

- (53) Pan, Q. -Q.; Li, S. -B.; Wu, Y.; Sun, G. -Y.; Geng, Y.; Su, Z. -M. A comparative study of a fluorene-based non-fullerene electron acceptor and PC61BM in an organic solar cell at a quantum chemical level. *RSC Adv.* **2016**, *6*, 81164-81173.
- (54) Lu, T.; Chen, F. Multiwfn: a multifunctional wavefunction analyzer. *J. Comput. Chem.* **2012**, *33*, 580-592.
- (55) Gaussian 16, Revision C.01, Frisch, M. J.; Trucks, G. W.; Schlegel, H. B.; Scuseria, G. E.; Robb, M. A.; Cheeseman, J. R.; Scalmani, G.; Barone, V.; Petersson, G. A.; Nakatsuji, H.; Li, X.; Caricato, M.; Marenich, A. V.; Bloino, J.; Janesko, B. G.; Gomperts, R.; Mennucci, B.; Hratchian, H. P.; Ortiz, J. V.; Izmaylov, A. F.; Sonnenberg, J. L.; Williams-Young, D.; Ding, F.; Lipparini, F.; Egidi, F.; Goings, J.; Peng, B.; Petrone, A.; Henderson, T.; Ranasinghe, D.; Zakrzewski, V. G.; Gao, J.; Rega, N.; Zheng, G.; Liang, W.; Hada, M.; Ehara, M.; Toyota, K.; Fukuda, R.; Hasegawa, J.; Ishida, M.; Nakajima, T.; Honda, Y.; Kitao, O.; Nakai, H.; Vreven, T.; Throssell, K.; Montgomery, J. A.; Peralta, J. E.; Ogliaro, F.; Bearpark, M. J.; Heyd, J. J.; Brothers, E. N.; Kudin, K. N.; Staroverov, V. N.; Keith, T. A.; Kobayashi, R.; Normand, J.; Raghavachari, K.; Rendell, A. P.; Burant, J. C.; Iyengar, S. S.; Tomasi, J.; Cossi, M.; Millam, J. M.; Klene, M.; Adamo, C.; Cammi, R.; Ochterski, J. W.; Martin, R. L.; Morokuma, K.; Farkas, O.; Foresman, J. B., Fox, D. J. Gaussian, Inc., Wallingford CT, **2019**.
- (56) Blouin, N.; Michaud, A.; Gendron, D.; Wakim, S.; Blair, E.; Neagu-Plesu, R.; Belletete, M.; Durocher, G.; Tao, Y.; Leclerc, M. Toward a Rational Design of Poly(2,7-Carbazole) Derivatives for Solar Cells. *J. Am. Chem. Soc.* **2008**, *130*, 732-742.
- (57) Dong, H.; Wang, C.; Hu, W. High performance organic semiconductors for field-effect transistors. *Chem. Commun.* **2010**, *46*, 5211-5222.
- (58) Scharber, M. C.; Muhlbacher, D.; Koppe, M.; Denk, P.; Waldauf, C.; Heeger, A. J.; Brabec, C. J. Design rules for donors in bulk-heterojunction solar cells-Towards 10% energy-conversion efficiency. *Adv. Mater.* **2006**, *18*, 789-794.
- (59) Qi, B.; Wang, J. Fill Factor in Organic Solar Cells. *Phys. Chem. Chem. Phys.* **2013**, *15*, 8972-8982.
- (60) Green, M. A. Solar Cell Fill Factors: General Graph And Empirical Expressions. *Solid-State Electron.* **1981**, *24*, 788-789.
- (61) Fu, Z.; Shen, W.; He, R.; Liu, X.; Sun, H.; Yin, W.; Li, M. Theoretical Studies on the Effect of a Bithiophene Bridge with Dierent Substituent Groups (R = H, CH₃, OCH₃ and CN) in Donor- π -acceptor Copolymers for Organic Solar Cell Applications. *Phys. Chem. Chem. Phys.* **2015**, *17*, 2043-2053.
- (62) Peumans, P.; Yakimov, A.; Forrest, S. R. Small Molecular Weight Organic Thin-film Photodetectors and Solar Cells. *J. Appl. Phys.* **2003**, *93*, 3693-3723.
- (63) Berube, N.; Gosselin, V.; Gaudreau, J.; Cote, M. Designing Polymers for Photovoltaic Applications Using ab Initio Calculations. *J. Phys. Chem. C* **2013**, *117*, 7964-7972.
- (64) Li, G.; Zhu, R.; Yang, Y. Polymer Solar Cells. *Nat. Photonics* **2012**, *6*, 153-161.

- (65) Jiang, B. H.; Wang, Y. P.; Liao, C. Y.; Chang, Y. M.; Su, Y. W.; Jeng, R. J.; Chen, C. P. Improved blend film morphology and free carrier generation provide a high-performance ternary polymer solar cell. *ACS Appl. Mater. Interfaces* **2021**, *13*, 1076-1085.
- (66) Yan, C.; Tang, H.; Ma, R.; Zhang, M.; Liu, T.; Lv, J.; Huang, J.; Yang, Y.; Xu, T.; Kan, Z.; Yan, H.; Liu, F.; Lu, S.; Li, G. Synergy of liquid-crystalline small-molecule and polymeric donors delivers uncommon morphology evolution and 16.6% efficiency organic photovoltaics. *Adv. Sci. (Weinh)* **2020**, *7*, 2000149.
- (67) Guo, M.; He, R.; Dai, Y.; Shen, W.; Li, M.; Zhu, C.; Lin, S. H. Electron-Deficient Pyrimidine Adopted in Porphyrin Sensitizers: A Theoretical Interpretation of π -Spacers Leading to Highly Efficient Photo-to-Electric Conversion Performances in Dye-Sensitized Solar Cells. *J. Phys. Chem. C* **2012**, *116*, 9166-9179.
- (68) Cioni, I.; Bahers, T. L.; Adamo, C.; Odobel, F.; Jacquemin, D. Through-Space Charge Transfer in Rod-Like Molecules: Lessons from Theory. *J. Phys. Chem. C* **2012**, *116*, 11946-11955.
- (69) Clarke, T. M.; Durrant, J. R. Charge Photogeneration in Organic Solar Cells. *Chem. Rev.* **2010**, *110*, 6736-6767.
- (70) Kose, M. E.; Mitchell, W. J.; Kopidakis, N.; Chang, C. H.; Shaheen, S. E.; Kim, K.; Rumbles, G. Theoretical Studies on Conjugated Phenyl-Cored Thiophene Dendrimers for Photovoltaic Applications. *J. Am. Chem. Soc.* **2007**, *129*, 14257-14270.
- (71) Jin, J. -L.; Li, H. -B.; Geng, Y.; Wu, Y.; Duan, Y. -A.; Su, Z. -M. Theoretical Insight into the Origin of Large Stokes Shift and Photophysical Properties of Anilido-Pyridine Boron Diuride Dyes. *ChemPhysChem* **2012**, *13*, 3714-3722.
- (72) Liu, C. -C.; Mao, S. -W.; Kuo, M. -Y. Cyanated Pentaceno[2,3-*c*]chalcogenophenes for Potential Application in Air-Stable Ambipolar Organic Thin-Film Transistors. *J. Phys. Chem. C* **2010**, *114*, 22316-22321.
- (73) Khatua, R.; Debata, S.; Sahu S. Computational characterization of N-type characteristics and optoelectronic properties in air-stable pyromellitic diimide derivatives. *New J. Chem.* **2020**, *44*, 8412-8421.
- (74) Cui, Y.; Zhu, P.; Shi, X.; Liao, X.; Chen, Y. Theoretical Study of Excited State Charge Transfer Characteristics based on A-D-A and A-DA'D-A Type Nonfullerene Acceptors. *J. Phys. Chem. C* **2021**, *125*, 10250-10259.
- (75) Huang, W.; Xie, W.; Huang, H.; Zhang, H.; Liu, H. Designing organic semiconductors with ultrasmall reorganization energies: insights from molecular symmetry, aromaticity and energy gap. *J. Phys. Chem. Lett.* **2020**, *11*, 4548-4553.
- (76) Siddiqui, S. A. In silico investigation of the coumarin-based organic semiconductors for the possible use in organic electronic devices. *J. Phys. Org. Chem.* **2019**, *32*, e3905.
- (77) Vidya, V. M.; Tripathi, A.; Prabhakar, C. Linear, non-linear optical properties and reorganization energies of d- π -a star-shaped triazine derivatives: A DFT study. *J. Mol. Struct.* **2019**, *1176*, 855-864.

- (78) Sahu, H.; Panda, A. N. Computational investigation of charge injection and transport properties of a series of thiophenepyrrole based oligo-azomethines. *Phys. Chem. Chem. Phys.* **2014**, *16*, 8563-8574.
- (79) Marcus, R. A. On the Theory of Electron Transfer Reactions. VI. Unified Treatment for Homogeneous and Electrode Reactions. *J. Chem. Phys.* **1965**, *43*, 679-701.
- (80) Marcus, R. A. Electron Transfer Reactions in Chemistry. Theory and Experiment. *Rev. Mod. Phys.* **1993**, *65*, 599-610.
- (81) Newton, M. D. Quantum chemical probes of electron-transfer kinetics: the nature of donor-acceptor interactions. *Chem. Rev.* **1991**, *91*, 767-792.
- (82) Wen, S. -H.; Li, A.; Song, J.; Deng, W. -Q.; Han, K. -L.; Goddard, W. A. First-principles investigation of anisotropic hole mobilities in organic semiconductors. *J. Phys. Chem. B* **2009**, *113*, 8813-8819.
- (83) Deng, W. Q.; Sun, L.; Huang, J. D.; Chai, S.; Wen, S. H.; Han, K. L. Quantitative prediction of charge mobilities of π -stacked systems by first-principles simulation. *Nat. Prot.* **2015**, *10*, 632-642.
- (84) Wang, T.; Bredas, J. -L. Organic solar cells based on non-fullerene small-molecule acceptors: impact of substituent position. *Matter* **2020**, *2*, 119-135.
- (85) Guido, C. A.; Cortona, P.; Mennucci, B.; Adamo C. On the metric of charge transfer molecular excitations: a simple chemical descriptor. *J. Chem. Theory Comput.* **2013**, *9*, 3118-3126.

Supporting Information

Computational Design of Crescent Shaped Promising Non-Fullerene Acceptors with 2,3-quinoxaline,1,4-dihydro Core and Different Electron-withdrawing Terminal Units for Photovoltaic Applications

Labanya Bhattacharya,¹Alex Brown², Sagar Sharma,³ and Sridhar Sahu^{1*}

¹*Computational Materials Research Lab, Department of Physics, Indian Institute of Technology (Indian School of Mines), Dhanbad, Jharkhand-826004, India*

²*Department of Chemistry, University of Alberta, Edmonton, Alberta, T6G 2G2, Canada*

³*Department of Chemistry, S. B. Deorah College, Bora Service, Ulubari, Guwahati-781007, Assam, India*

E-mail: *sridharsahu@iitism.ac.in

CONTENTS

Theory

Section S.1. Crystal structure prediction

Section S.2. Theory related to charge transfer integral, charge transfer rate and anisotropic mobility

Section S.3. References

List of Tables

Table S1. The HOMO energy levels in eV of AQx-2 in the gas phase as determined using several functionals with the 6-31G(d,p) and 6-311G(d,p) basis sets

Table S2. Computed HOMO, LUMO energies and optical band gap ($E_{g,opt}$) of PM6 polymer donor at B3LYP-D3BJ/6-31G(d,p) theoretical level in the gas phase

Table S3. The maximum optical absorption wavelength (λ_{abs}) of AQx-2 in Chloroform solvent medium using several functionals with the 6-31G(d,p) basis set. All the computations at the B3LYP-D3BJ/6-31G(d,p) optimized geometry

Table S4. Dihedral angles (α, β, γ) in degrees and bond lengths (d_1, d_2, d_3, d_4) in Å of the designed NFAs as determined at the B3LYP-D3BJ/6-31G(d,p) level of theory in the gas phase

Table S5. Charge injection barriers in eV of the designed NFAs w.r.t Al electrode

Table S6. Computed electronic transition energy E (eV), absorption wavelength λ_{abs} (nm), major configurations, oscillator strength (f), and light harvesting efficiency (η_λ) of the designed NFAs as determined at the B3LYP-D3BJ/6-31G(d,p) level of theory in the solvent (Chloroform) phase

Table S7. Space group and simulated unit cell parameters (a, b, c in Å and α , β , γ in deg) of the studied NFAs.

Table S8. Intermolecular charge transfer (CT) states, excitation energy (E), absorption wavelength (λ_{abs}), oscillator strength (f), Δr index, contribution rate of the main NTO pairs for the investigated PM6 donor-NFA blends or complexes at the CAM-B3LYP/6-31G(d,p) level of theory in solvent (Chloroform) phase

List of Figures

Figure S1. HOMO, LUMO energies and optical band gap ($E_{\text{g,opt}}$) of PM6 polymer donor at B3LYP-D3BJ/6-31G(d,p) theoretical level in the gas phase.

Figure S2. Molecular electrostatic potential (MEP) maps of the designed NFAs.

Figure S3. The contour plots of FMOs of the designed NFAs (AQx-2, AQx-2-c, AQx-2-ct1, AQx-2-ct2, and AQx-2-ct3; isosurface value= 0.02 a.u.) at the B3LYP-D3BJ/6-31G(d,p) level of theory.

Figure S4. The contour plots of FMOs of the designed NFAs (AQx-2-ct4, AQx-2-ct5, AQx-2-ct6, AQx-2-ct7 and AQx-2-ct8; isosurface value= 0.02 a.u.) at the B3LYP-D3BJ/6-31G(d,p) level of theory.

Figure S5. Simulated charge density difference ($\Delta\rho$) plots associated with the $S_0 \rightarrow S_1$ transition of the studied NFAs at the CAM-B3LYP/6-31G(d,p) level of theory in Chloroform solvent (isosurface value 0.0002 a.u.). The green and blue regions correspond to positive and negative regions, respectively

Figure S6. Extending zones for the centroids C+/C- associated with the $S_0 \rightarrow S_1$ transition of the studied NFAs at the CAM-B3LYP/6-31G(d,p) level of theory in Chloroform solvent (isosurface value 0.0002 a.u.). The green and blue regions correspond to positive and negative regions, respectively

Figure S7. Simulated transition density matrix (TDM) at the CAM-B3LYP/6-31G(d,p) level of theory associated with the $S_0 \rightarrow S_1$ transition of the studied NFAs (AQx-2, AQx-2-ct1, AQx-2-ct2, AQx-2-ct3, AQx-2-ct4, and AQx-2-ct5) in Chloroform solvent (the hydrogen atoms of all molecular systems are omitted) and the color bars are given on the right

Figure S8. Simulated transition density matrix (TDM) at the CAM-B3LYP/6-31G(d,p) level of theory associated with the $S_0 \rightarrow S_1$ transition of the studied NFAs (AQx-2-ct6, AQx-2-ct7, and AQx-2-ct8) in Chloroform solvent (the hydrogen atoms of all molecular systems are omitted) and the color bars are given on the right

Figure S9. The atom numbering of the designed NFAs (NFA:AQx-2-c) corresponding to TDM mapping. The cyan, yellow, blue, red and greenish yellow represents carbon, sulfur, nitrogen, oxygen and fluorine atoms, respectively.

Figure S10. Simulated crystal structures showing different hopping channels and angle resolved anisotropic mobility of the studied NFAs (AQx-2-ct1, AQx-2-ct2)

Figure S11. Simulated crystal structures showing different hopping channels and angle resolved anisotropic mobility of the studied NFAs (**AQx-2-ct4**, and **AQx-2-ct5**)

Figure S12. Simulated crystal structures showing different hopping channels and angle resolved anisotropic mobility of the studied NFAs (**AQx-2-ct6**, **AQx-2-ct7**, and **AQx-2-ct8**)

Figure S13. The NTO analysis of the CT excited states of the investigated PM6/NFA (**AQx-2-ct1**, **AQx-2-ct2**, **AQx-2-ct4**, **AQx-2-ct5**) blends. The blue and red colors represent the positive and negative isosurfaces, respectively

Figure S14. The NTO analysis of the CT excited states of the investigated PM6/NFA (**AQx-2-ct6**, **AQx-2-ct7**, **AQx-2-ct8**) blends. The blue and red colors represent the positive and negative isosurfaces, respectively

Theory

S.1. Crystal Structure Prediction

Crystal structures of the designed NFAs have been predicted employing the most reliable Dreiding force field within the Polymorph Predictor module of the BIOVIA Materials Studio17 based on their optimized gas-phase conformations. During computation, the Polymorph Predictor quality is set to default fine settings, which anneals the sample in Monte Carlo simulation algorithm within a temperature ranges from 300.0 K to 100000.0 K, and a heating factor of 0.025. The maximum no of steps is 7000 and before cooling, 12 successive steps are accepted. All possible crystal structures of the studied NFAs are selected by energy minimization of crystals with the most common space groups such as $P2_1/C$, $P1$, $P\bar{1}$, $Pbca$, $P2_12_12_1$, $P2_1$, $C2/c$, $Pna2_1$, Cc , $Pbcn$, and $C2$ as registered in Cambridge Structural Database (CSD) [1, 2, 3]. For every NFA, the structure with the lowest lattice energy has been selected for further calculations.

S.2. Theory related to charge transfer integral, charge transfer rate, and anisotropic mobility

S.2.1. Charge transfer rate:

Based on Marcus Theory, the electron and hole transport in an organic semiconductor material can be described by the hoping mechanism. For the self-exchange transfer reaction where the neighboring molecules are equivalent, the free energy difference (ΔG) is nearly equal to zero. The rate of charge transfer (K) rate for electron (e) and hole (h) transport can be represented as [4, 5, 6],

$$k_{h/e} = \frac{2\pi V^2}{h} \left(\frac{\pi}{\lambda k_B T}\right)^{1/2} \exp\left(-\frac{\lambda}{4k_B T}\right) \quad (1)$$

In the above equation, V is the charge transfer integral, λ is the reorganization energy, k_B is the Boltzmann constant, and T is the temperature ($T=300$ K).

S.2.2 Charge transfer integral:

Charge transfer integrals are calculated based on the direct coupling (DC) method. The charge transfer integrals estimated using this method can provide more accurate results as this method

takes into account the nonzero spatial overlap between the molecular orbitals of neighbor molecules [7, 8]. In the direct coupling method, the hole transfer integral or electron transfer integral is computed as,

$$V_{h/e} = \frac{J - S(e_1 + e_2)/2}{1 - S^2} \quad (2)$$

where J is the charge transfer integral, S is the overlap integral, and e_1, e_2 , are the site energies of fragment 1 and 2, of the molecular dimer, respectively. The electronic coupling terms J, S, e_1 , and e_2 can be defined as;

$$J = \langle \varphi_1 | H_{KS} | \varphi_2 \rangle \quad (3)$$

$$S_{12} = \langle \varphi_1 | \varphi_2 \rangle \quad (4)$$

$$e_1 = \langle \varphi_1 | H_{KS} | \varphi_1 \rangle \quad (5)$$

$$e_2 = \langle \varphi_2 | H_{KS} | \varphi_2 \rangle \quad (6)$$

In the electron transfer integral calculations, φ_1 is the LUMO of fragment 1, and φ_2 is the LUMO of fragment 2. Similarly, for the hole transport, φ_1 is the HOMO of fragment 1, and φ_2 is the HOMO of fragment 2.

S.2.3 Reorganization energy:

The internal reorganization (λ_i) energies of all the investigated NFAs during hole, and electron transfer are evaluated using the adiabatic potential energy surface (APS) method. Using that method, the internal reorganization energy for the hole (λ_h) and electron (λ_e) transfer can then be described as [6];

$$\lambda_h = [E^+(M^0) - E^+(M^+)] + [E^0(M^+) - E^0(M^0)] \quad (7)$$

$$\lambda_e = [E^0(M^-) - E^0(M^0)] + [E^-(M^0) - E^-(M^-)] \quad (8)$$

The minimum energy of the neutral state is described as $E^0(M^0)$, and for cationic and anionic states, the minimum energies are $E^+(M^+)$ and $E^-(M^-)$, respectively. During the charge transfer process, geometry changes arise in four possible energy states such as $E^-(M^0)$, $E^+(M^0)$, $E^0(M^+)$, and $E^0(M^-)$. The $E^-(M^0)$ and $E^+(M^0)$ are the total energy of the anionic/cationic states with the geometries of the neutral species. The $E^0(M^+)$ and $E^0(M^-)$ define the total energy of the neutral state with respect to the geometry of cationic/anionic species.

S.2.4 Anisotropic Mobility:

At high temperature, the charge transport in the disordered organic crystals is found to be anisotropic in nature, because of the increased fluctuations in the intermolecular interactions. The angular resolution anisotropic mobility (μ_ϕ) in organic crystals is subject to the molecular packing in a particular plane. In accordance with the Einstein relation, the anisotropic mobility (μ_ϕ) can be evaluated as [9, 10],

$$\mu_{\varphi} = \frac{e}{2k_B T} \sum_i k_i r_i^2 P_i \cos^2 \gamma_i \cos^2 (\theta_i - \varphi) \quad (9)$$

In the above equation, r_i is the intermolecular distance associated with i 'th hopping pathway and P_i is the hopping probability of the transport channel. γ_i is the angle made by the corresponding hopping pathways with respect to the basal plane of the dimers. θ_i is the angle of the hopping path relative to the crystallographic axis, φ is the angle of orientation of the conducting channel relative to the crystallographic axis and $(\theta_i - \varphi)$ denotes the angle between the conducting channel and hopping pathway.

References

1. Mighell, A. D.; Ondik, H. M.; Molino., B. B. Crystal data space-group tables. *J. Phys. Chem. Ref. Data* **1977**, *6*, 675.
2. Mahmood, A.; Tang, A.; Wang, X.; Zhou, E. First-principles theoretical designing of planar non-fullerene small molecular acceptors for organic solar cells: manipulation of noncovalent interactions. *Phys. Chem. Chem. Phys.* **2019**, *21*, 2128-2139.
3. Debata, S.; Sahoo, S. R.; Khatua, R.; Sahu, S. Rational design and crystal structure prediction of ring-fused double-PDI compounds as n-channel organic semiconductors: a DFT study. *Phys. Chem. Chem. Phys.* **2021**, *23*, 12329-12339.
4. Marcus, R. A. On the Theory of Electron Transfer Reactions. VI. Unified Treatment for Homogeneous and Electrode Reactions. *J. Chem. Phys.* **1965**, *43*, 679-701.
5. Marcus, R. A. Electron Transfer Reactions in Chemistry. Theory and Experiment. *Rev. Mod. Phys.* **1993**, *65*, 599-610.
6. Sahu, H.; Panda, A. N. Computational investigation of charge injection and transport properties of a series of thiophene-pyrrole based oligo-azomethines. *Phys. Chem. Chem. Phys.* **2014**, *16*, 8563-8574.
7. Senthilkumar, K. Grozema, F. C. Bickelhaupt, F. M. Siebbeles, L. D. A. Charge transport in columnar stacked triphenylenes: Effects of conformational fluctuations on charge transfer integrals and site energies. *J. Chem. Phys.* **2003**, *119*, 9809-9817.
8. Newton, M. D. Quantum chemical probes of electron-transfer kinetics: the nature of donor-acceptor interactions. *Chem. Rev.* **1991**, *91*, 767-792.
9. Wen, S. -H.; Li, A.; Song, J.; Deng, W. -Q.; Han, K. -L. Goddard, W. A. First-principles investigation of anisotropic hole mobilities in organic semiconductors. *J. Phys. Chem. B* **2009**, *113*, 8813-8819.
10. Deng, W. Q.; Sun, L.; Huang, J. D.; Chai, S.; Wen, S. H.; Han, K. L. Quantitative prediction of charge mobilities of π -stacked systems by first-principles simulation. *Nat. Prot.* **2015**, *10*, 632-642.

Table S1. The HOMO energy levels in eV of AQx-2 in the gas phase as determined using several functionals with the 6-31G(d,p) and 6-311G(d,p) basis sets.

Method	Basis set		Exp.
	6-31G(d,p)	6-311G(d,p)	
B3LYP	-5.51	-5.75	-5.62
B3LYP-D3BJ	-5.52	-5.76	
PBE0	-5.73	-5.91	
MPW91PW91	-5.75	-5.93	
M06	-5.80	-6.01	
ω B97XD	-7.10	-7.29	

Table S2. Computed HOMO, LUMO energies and optical band gap ($E_{g,opt}$) of PM6 polymer donor at B3LYP-D3BJ/6-31G(d,p) theoretical level in the gas phase

Degree of polym. (n)	HOMO (eV)	LUMO (eV)	$E_{g,opt}$ (eV)	LUMO (HOMO+ $E_{g,opt}$) (eV)
1	-5.15	-2.46	2.33	-2.82
2	-5.02	-2.66	2.01	-3.01
3	-4.98	-2.72	1.90	-3.08
4	-4.96	-2.75	1.87	-3.09
∞	-4.90	-2.84	1.78	-3.12

Table S3. The maximum optical absorption wavelength (λ_{abs}) of AQx-2 in Chloroform solvent medium using several functionals with the 6-31G(d,p) basis set. All the computations at the B3LYP-D3BJ/6-31G(d,p) optimized geometry

Method	State	λ_{abs} (nm)	Major. Conf.	Oscillator Strength (f)	Exp. data
B3LYP-D3BJ	$S_0 \rightarrow S_1$	716	H \rightarrow L (99%)	2.2623	732 nm
PBE0	$S_0 \rightarrow S_1$	684	H \rightarrow L (97%)	2.3916	
M06	$S_0 \rightarrow S_1$	681	H \rightarrow L (95%)	2.3614	
LC- ω PBE	$S_0 \rightarrow S_1$	528	H \rightarrow L (66%)	2.6689	
LC-BLYP	$S_0 \rightarrow S_1$	526	H \rightarrow L (65%)	2.6810	
CAM-B3LYP	$S_0 \rightarrow S_1$	587	H \rightarrow L (80%)	2.6644	
ω B97XD	$S_0 \rightarrow S_1$	566	H \rightarrow L (73%)	2.6738	

Table S4. Dihedral angles (α, β, γ) in degrees and bond lengths (d_1, d_2, d_3, d_4) in Å of the designed NFAs as determined at the B3LYP-D3BJ/6-31G(d,p) level of theory in the gas phase

Comp.	α	β	γ	d_1	d_2	d_3	d_4
AQx-2 (Ref.)	1.36	1.87	2.99	1.408	1.382	1.408	1.382
AQx-2-c	1.34	1.87	1.91	1.411	1.379	1.411	1.379
AQx-2-ct1	1.37	1.91	1.94	1.409	1.381	1.409	1.381
AQx-2-ct2	1.31	1.93	1.91	1.410	1.381	1.410	1.381
AQx-2-ct3	1.31	1.93	1.93	1.409	1.382	1.409	1.382
AQx-2-ct4	1.36	1.83	1.90	1.411	1.380	1.411	1.380
AQx-2-ct5	1.45	1.93	1.83	1.415	1.375	1.415	1.375
AQx-2-ct6	1.32	1.90	1.68	1.424	1.365	1.424	1.365
AQx-2-ct7	1.40	1.96	1.73	1.421	1.366	1.421	1.366
AQx-2-ct8	2.67	3.20	1.87	1.417	1.375	1.417	1.375

Table S5. Charge injection barriers in eV of the designed NFAs w.r.t Al electrode

Comp.	Hole injection barrier	Electron injection barrier
AQx-2 (Ref.)	1.22	0.63
AQx-2-c	1.41	0.41
AQx-2-ct1	1.46	0.32
AQx-2-ct2	1.35	0.44
AQx-2-ct3	1.41	0.35
AQx-2-ct4	1.33	0.49
AQx-2-ct5	1.25	0.68
AQx-2-ct6	0.98	1.11
AQx-2-ct7	1.24	0.80
AQx-2-ct8	1.47	0.64

Table S6. Computed electronic transition energy E (eV), absorption wavelength λ_{abs} (nm), major configurations, oscillator strength (f), and light harvesting efficiency (η_{λ}) of the designed NFAs as determined at the B3LYP-D3BJ/6-31G(d,p) level of theory in the solvent (Chloroform) phase

Compound	State	E (eV)	λ_{abs} (nm)	major config.	f	η_{λ}
AQx-2 (ref)	$S_0 \rightarrow S_1$	1.73	716	H \rightarrow L (99%)	2.2623	0.9945
	$S_0 \rightarrow S_7$	2.55	486	H-2 \rightarrow L (75%)	0.5170	
AQx-2-c	$S_0 \rightarrow S_1$	1.77	701	H \rightarrow L (98%)	2.0966	0.9920
	$S_0 \rightarrow S_8$	2.58	480	H-2 \rightarrow L (52%)	0.3434	
AQx-2-ct1	$S_0 \rightarrow S_1$	1.74	713	H \rightarrow L (98%)	2.1140	0.9923
	$S_0 \rightarrow S_9$	2.54	487	H-2 \rightarrow L (84%)	0.5382	
AQx-2-ct2	$S_0 \rightarrow S_1$	1.72	719	H \rightarrow L (98%)	2.2204	0.9940
	$S_0 \rightarrow S_5$	2.49	497	H-2 \rightarrow L (97%)	0.3917	
AQx-2-ct3	$S_0 \rightarrow S_1$	1.70	730	H \rightarrow L (98%)	2.2345	0.9942
	$S_0 \rightarrow S_5$	2.47	502	H-2 \rightarrow L (97%)	0.4211	
AQx-2-ct4	$S_0 \rightarrow S_1$	1.77	700	H \rightarrow L (98%)	2.2034	0.9937
	$S_0 \rightarrow S_5$	2.55	486	H-2 \rightarrow L (98%)	0.3830	
AQx-2-ct5	$S_0 \rightarrow S_1$	1.84	673	H \rightarrow L (98%)	1.7130	0.9806
	$S_0 \rightarrow S_5$	2.18	568	H \rightarrow L+2 (95%)	0.5074	
AQx-2-ct6	$S_0 \rightarrow S_1$	1.99	622	H \rightarrow L (99%)	1.7252	0.9812
	$S_0 \rightarrow S_5$	2.71	457	H-2 \rightarrow L (97%)	0.8332	
AQx-2-ct7	$S_0 \rightarrow S_1$	1.96	633	H \rightarrow L (99%)	1.8702	0.9865
	$S_0 \rightarrow S_5$	2.68	463	H-2 \rightarrow L (98%)	0.8750	
AQx-2-ct8	$S_0 \rightarrow S_1$	2.08	597	H-1 \rightarrow L (98%)	0.0407	
	$S_0 \rightarrow S_2$	2.14	579	H \rightarrow L (97%)	1.6399	0.9771
	$S_0 \rightarrow S_5$	3.07	404	H-2 \rightarrow L (90%)	0.6101	

Table S7. Space group and simulated unit cell parameters (a, b, c in Å and α , β , γ in deg) of the studied NFAs.

Compound	Space group	Lattice parameters					
		a	b	c	α	β	γ
AQx-2 (Ref.)	P2 ₁	19.86	18.68	12.77	90.00	109.00	90.00
AQx-2-c	P1	13.29	12.60	14.77	114.00	90.00	85.00
AQx-2-ct1	P1	13.74	15.03	12.48	66.54	79.89	90.24
AQx-2-ct2	P1	8.67	15.32	24.83	101.56	96.99	121.25
AQx-2-ct3	P1	13.54	16.21	14.68	124.36	108.21	86.12
AQx-2-ct4	P1	21.38	13.21	11.92	107.09	122.64	107.13
AQx-2-ct5	Pna2 ₁	25.40	19.21	18.08	90.00	90.00	90.00
AQx-2-ct6	P2 ₁	13.97	17.53	18.29	90.00	111.55	90.00
AQx-2-ct7	P $\bar{1}$	20.07	17.71	13.53	105.30	105.42	96.95
AQx-2-ct8	P $\bar{1}$	13.45	28.09	10.31	73.35	83.03	87.70

Table S8. Intermolecular charge transfer (CT) states, excitation energy (E), absorption wavelength (λ_{abs}), oscillator strength (f), Δr index, contribution rate of the main NTO pairs for the investigated PM6 donor-NFA blends or complexes at the CAM-B3LYP/6-31G(d,p) level of theory in solvent (Chloroform) phase

Complex	CT state	E (eV)	λ_{abs} (nm)	f	Δr (Å)	NTO contribution rate
PM6:AQx-2	S28	3.82	325	0.0375	8.4166	706 \rightarrow 707 (60.78%)
PM6:AQx-2-c	S38	4.10	302	0.0167	15.3715	714 \rightarrow 715 (91.01%)
PM6:AQx-2-ct1	S30	3.77	329	0.0621	6.1961	730 \rightarrow 731 (78.19%)
PM6:AQx-2-ct2	S29	3.75	331	0.0054	9.0764	740 \rightarrow 741 (81.22%)
PM6:AQx-2-ct3	S33	3.88	319	0.0546	8.0211	756 \rightarrow 757 (68.31%)
PM6:AQx-2-ct4	S30	3.86	321	0.0979	8.6461	700 \rightarrow 701 (62.93%)
PM6:AQx-2-ct5	S38	4.02	308	0.0891	6.8833	700 \rightarrow 701 (65.04%)
PM6:AQx-2-ct6	S23	3.88	320	0.0177	8.7614	682 \rightarrow 683 (83.69%)
PM6:AQx-2-ct7	S19	3.80	326	0.0096	7.4638	698 \rightarrow 699 (77.28%)
PM6:AQx-2-ct8	S30	4.27	290	0.0080	9.1777	632 \rightarrow 633 (82.82%)

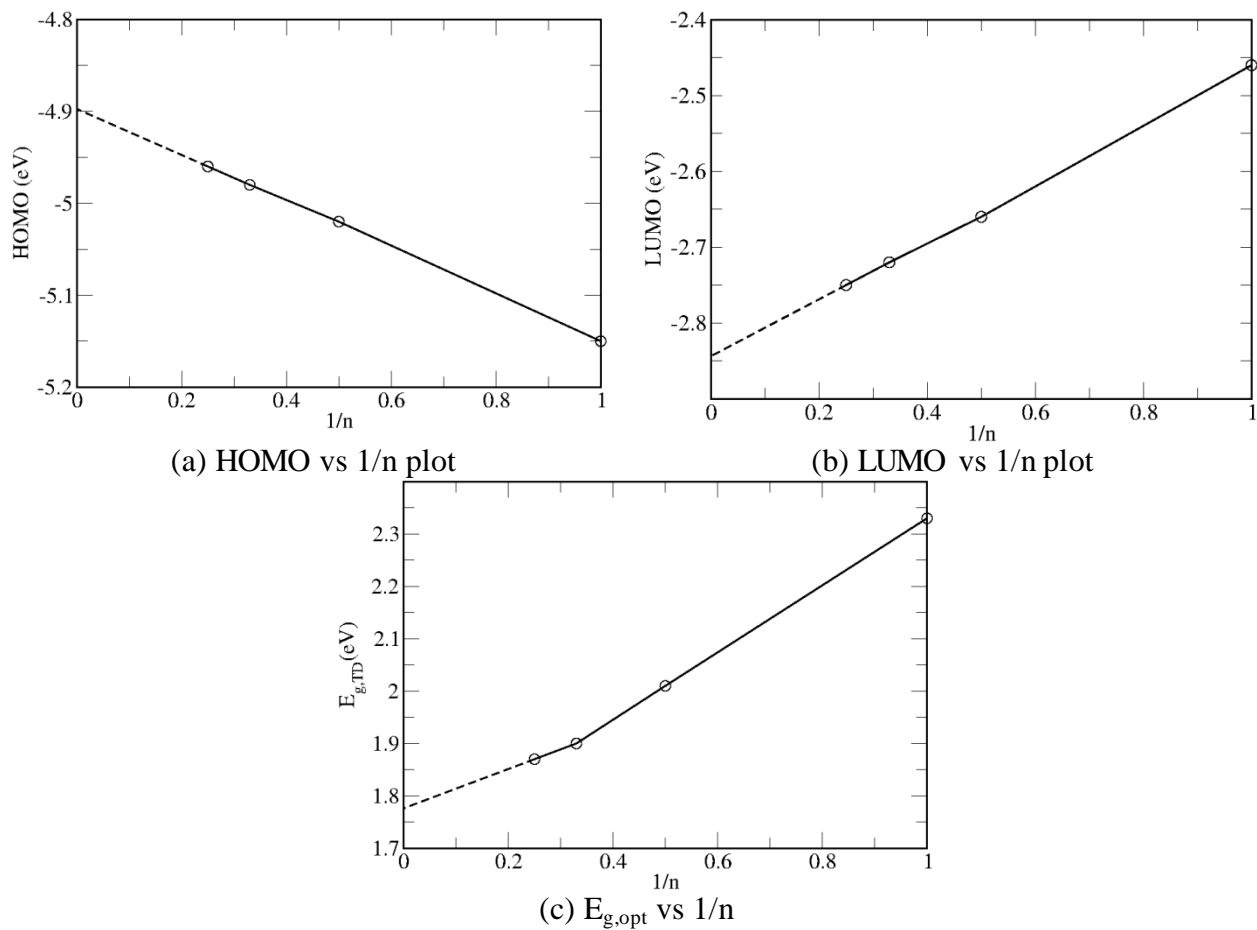
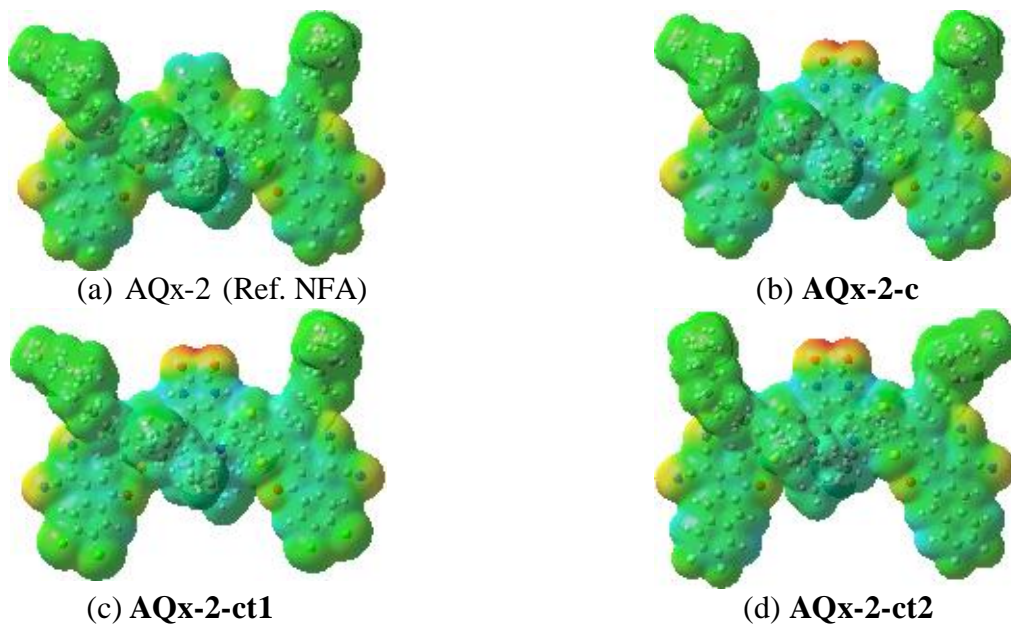


Figure S1. HOMO, LUMO energies and optical band gap ($E_{g,opt}$) of PM6 polymer donor at B3LYP-D3BJ/6-31G(d,p) theoretical level in the gas phase



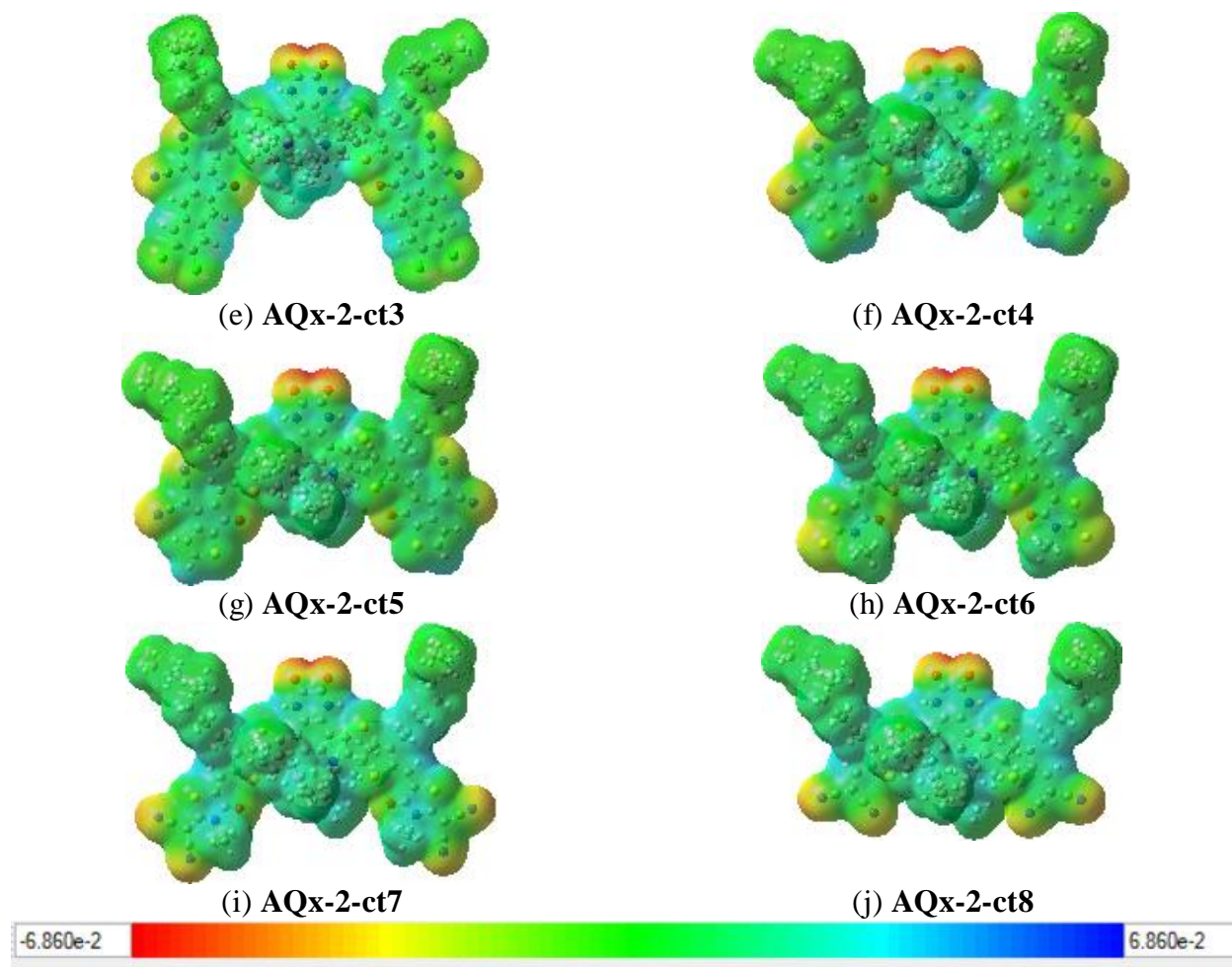
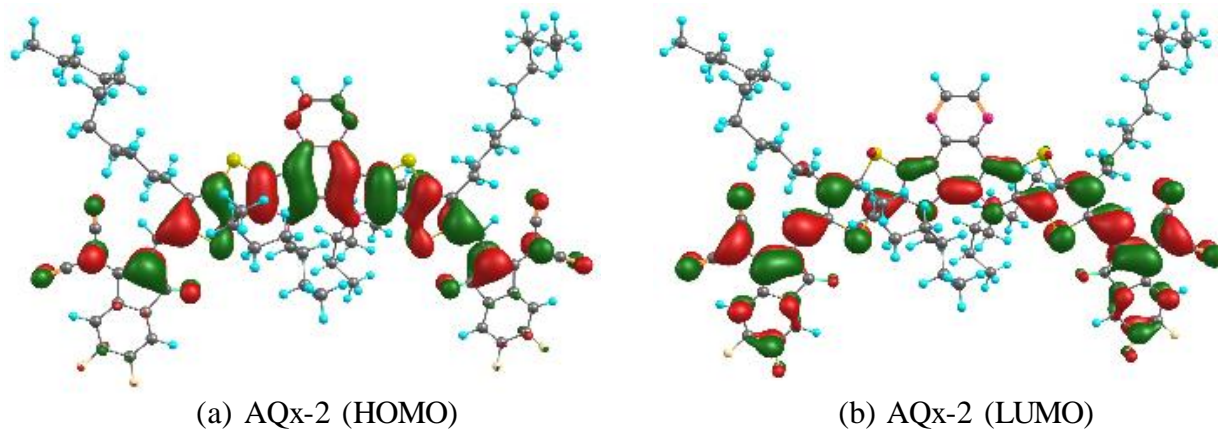
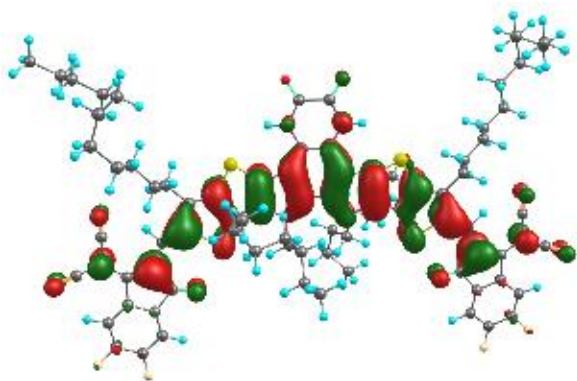
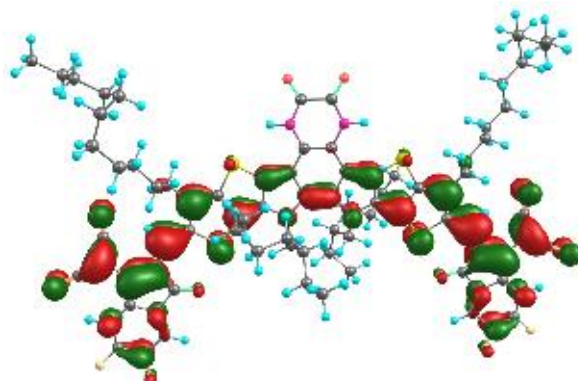


Figure S2. Molecular electrostatic potential (MEP) maps of the designed NFAs.

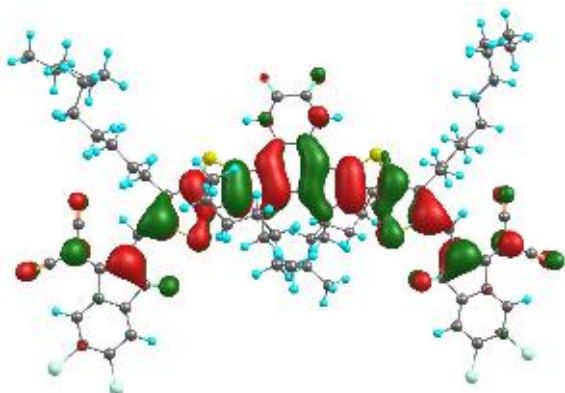




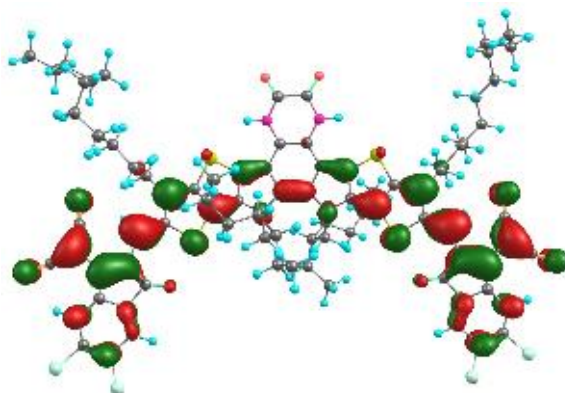
(C) AQx-2-c (HOMO)



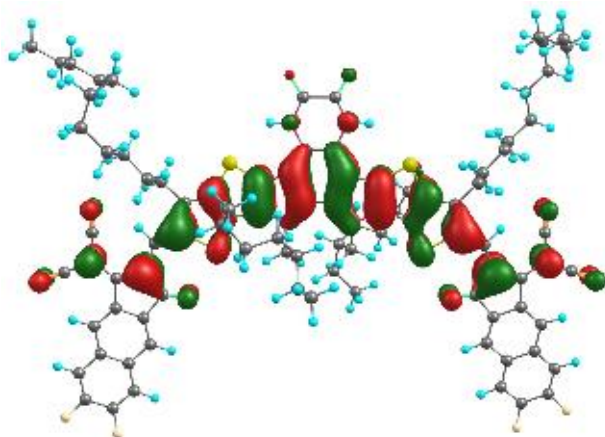
(d) AQx-2-c (LUMO)



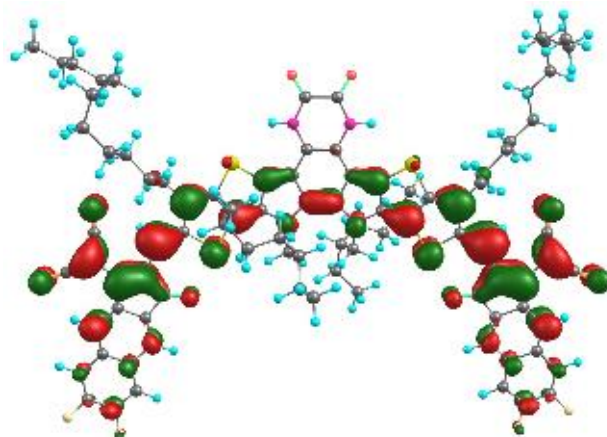
(e) AQx-2-ct1 (HOMO)



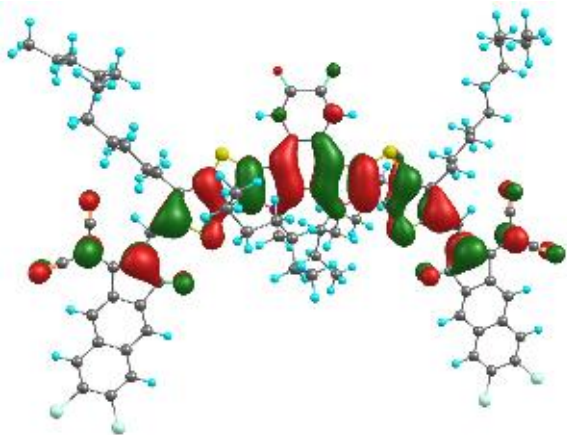
(f) AQx-2-ct1 (LUMO)



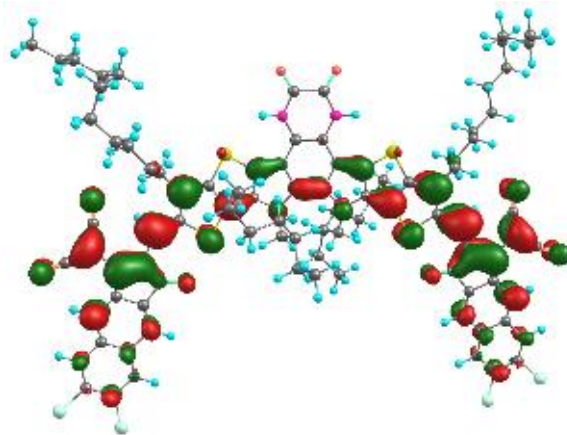
(g) AQx-2-ct2 (HOMO)



(h) AQx-2-ct2 (LUMO)

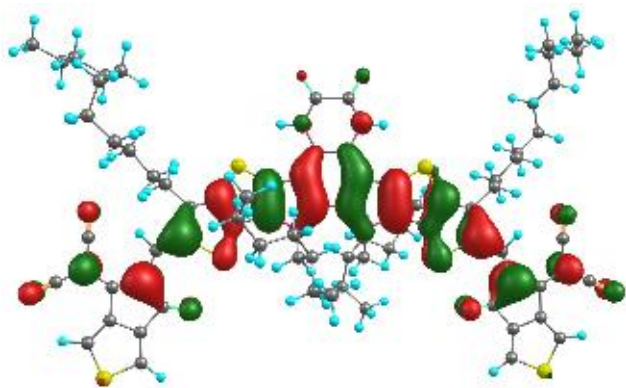


(i) AQx-2-ct3 (HOMO)

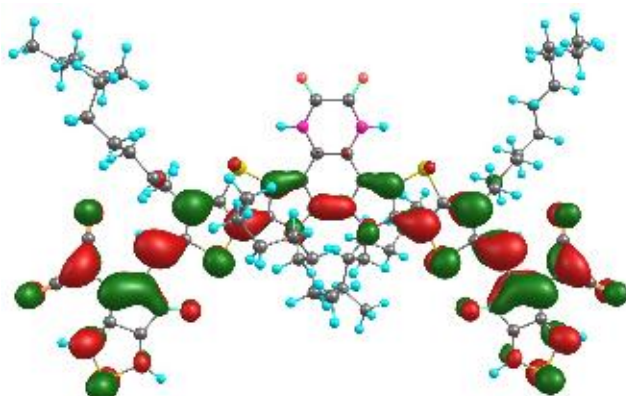


(j) AQx-2-ct3 (LUMO)

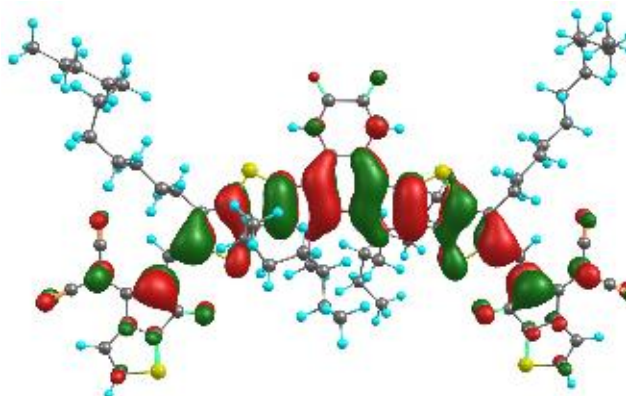
Figure S3. The contour plots of FMOs of the designed NFAs (AQx-2, AQx-2-c, AQx-2-ct1, AQx-2-ct2, and AQx-2-ct3; isosurface value= 0.02 a.u.) at the B3LYP-D3BJ/6-31G(d,p) level of theory.



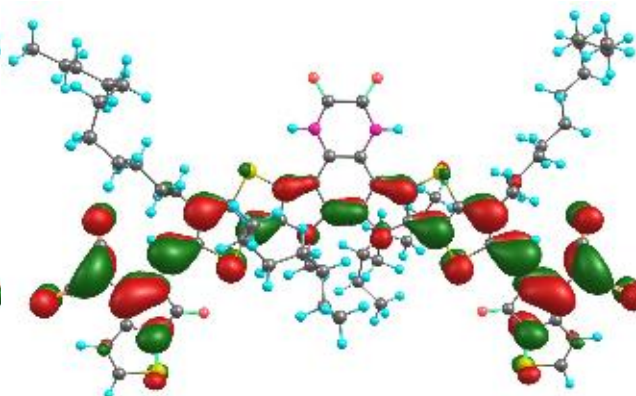
(a) AQx-2-ct4 (HOMO)



(b) AQx-2-ct4 (LUMO)



(c) AQx-2-ct5 (HOMO)



(d) AQx-2-ct5 (LUMO)

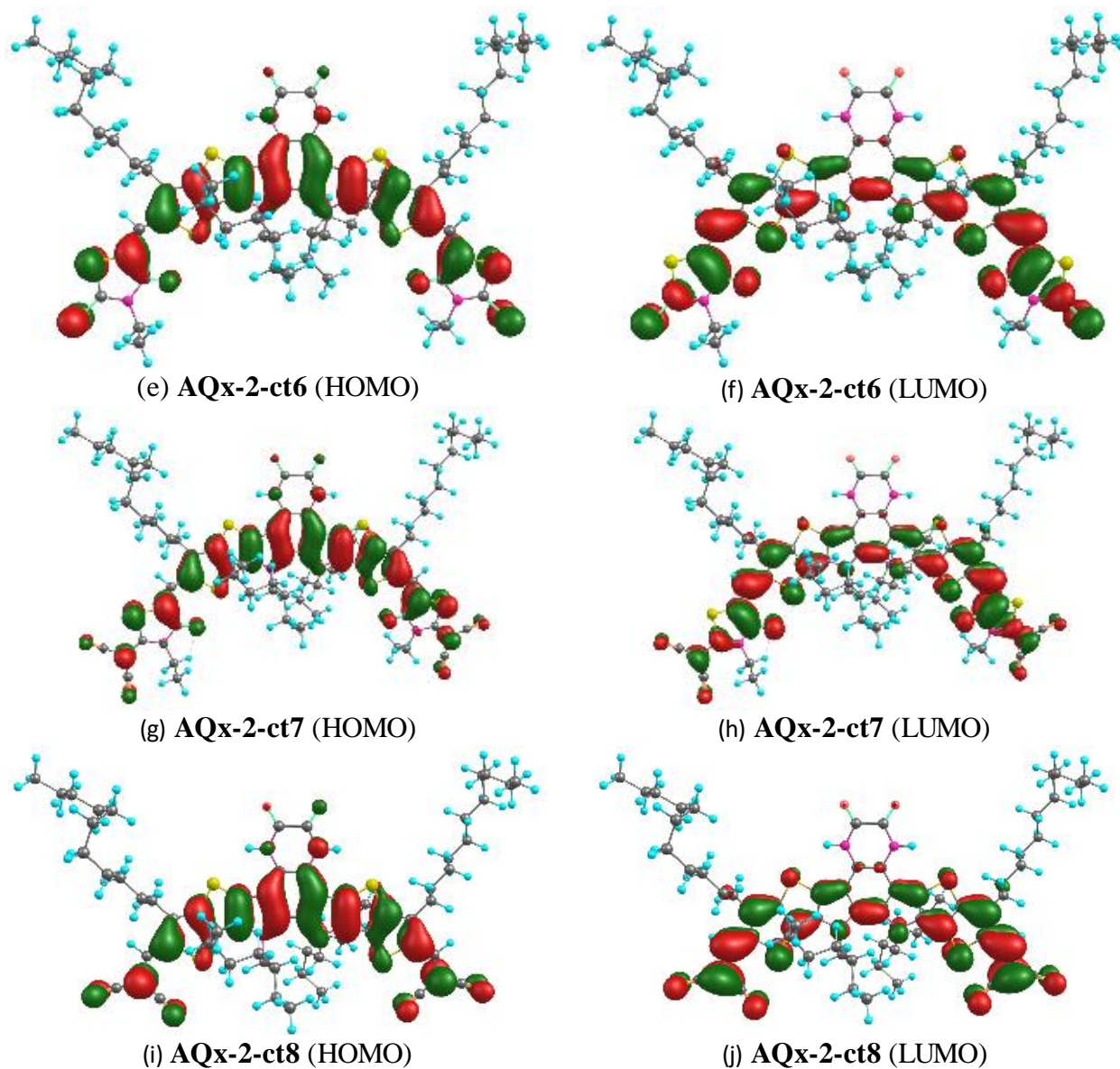


Figure S4. The contour plots of FMOs of the designed NFAs (AQx-2-ct4, AQx-2-ct5, AQx-2-ct6, AQx-2-ct7 and AQx-2-ct8; isosurface value= 0.02 a.u.) at the B3LYP-D3BJ/6-31G(d,p) level of theory

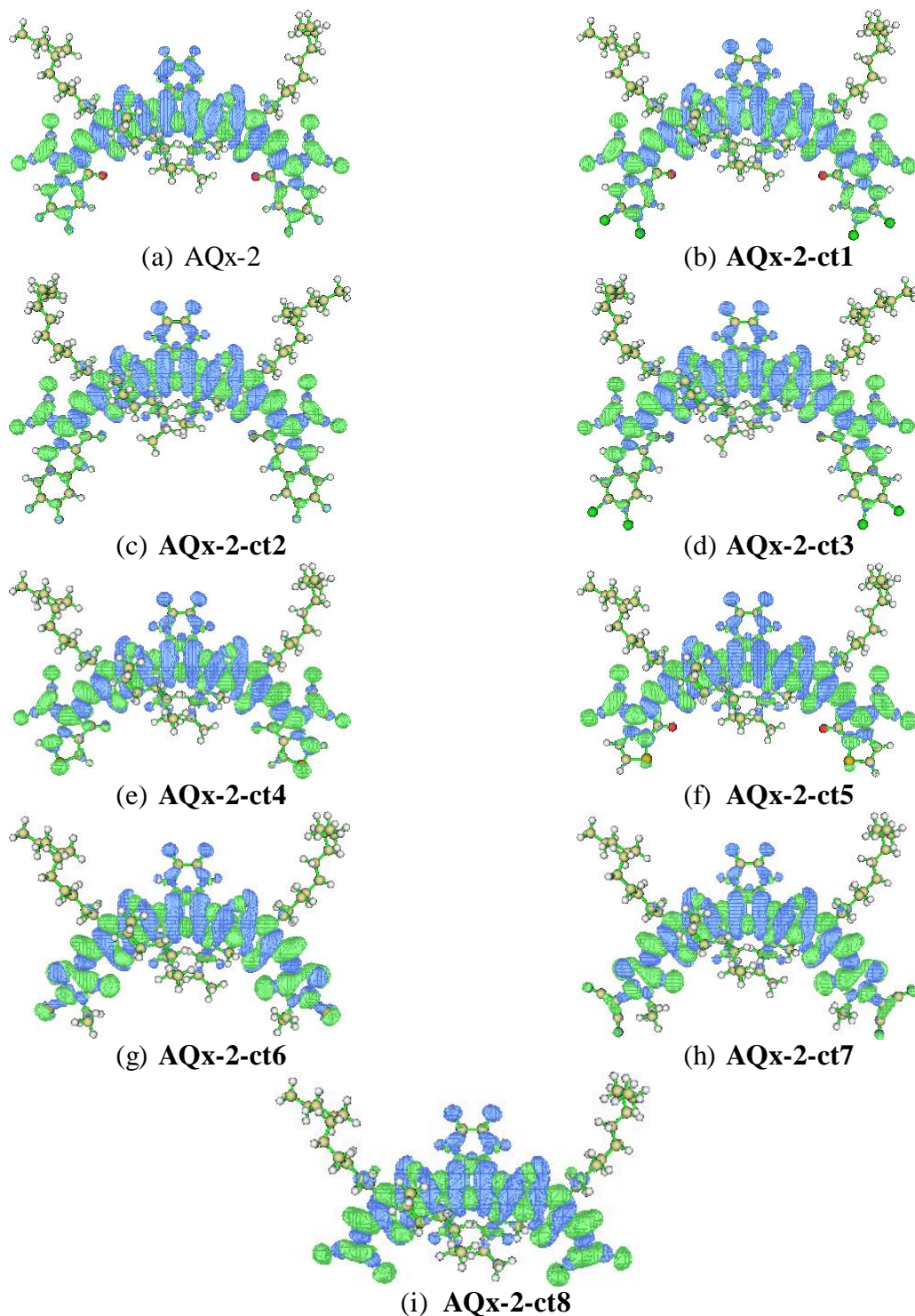


Figure S5. Simulated charge density difference ($\Delta\rho$) plots associated with the $S_0 \rightarrow S_1$ transition of the studied NFAs at the CAM-B3LYP/6-31G(d,p) level of theory in Chloroform solvent (isosurface value 0.0002 a.u.). The green and blue regions correspond to positive and negative regions, respectively

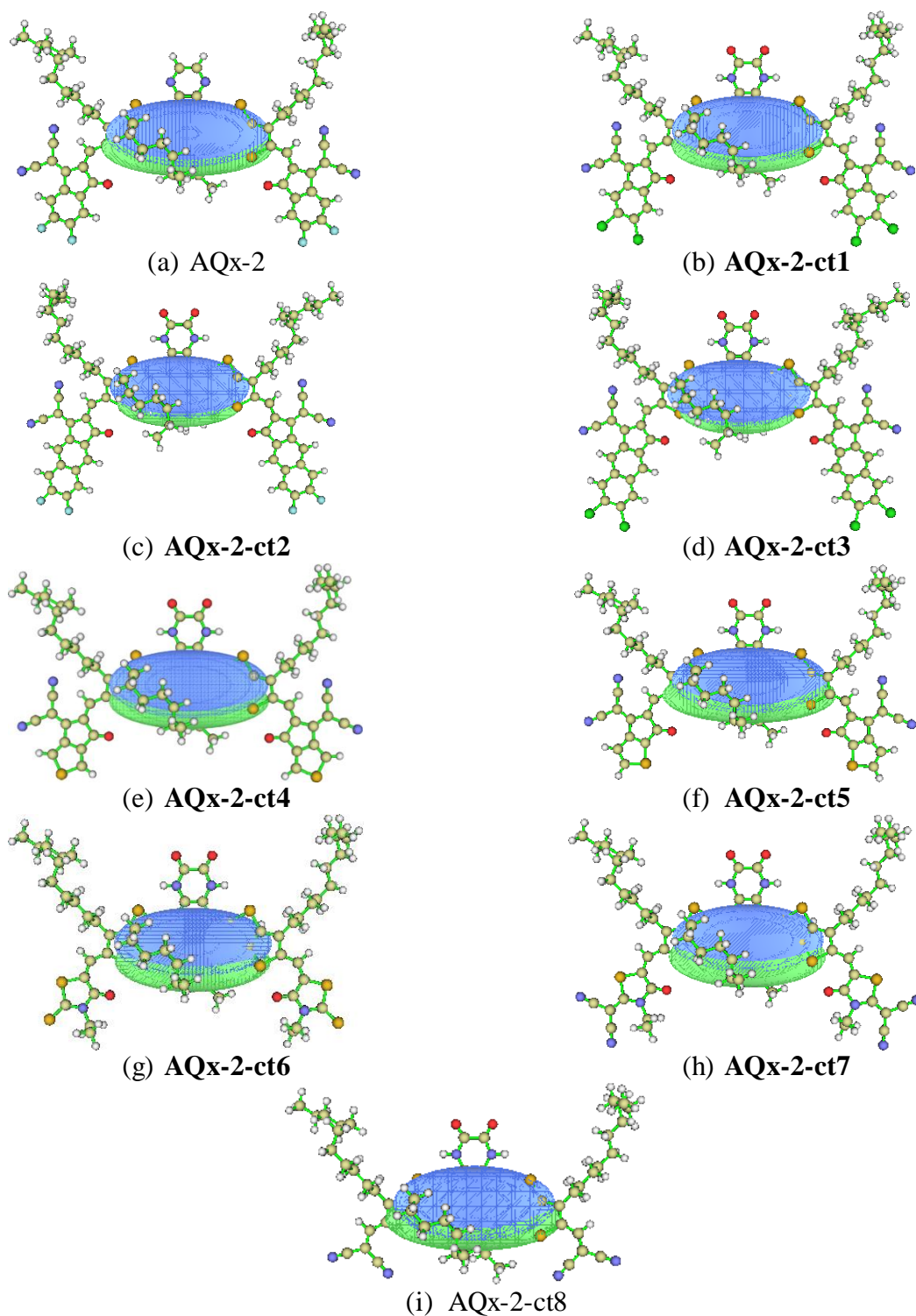


Figure S6. Extending zones for the centroids C⁺/C⁻ associated with the S₀→S₁ transition of the studied NFAs at the CAM-B3LYP/6-31G(d,p) level of theory in Chloroform solvent (isosurface value 0.0002 a.u.). The green and blue regions correspond to positive and negative regions, respectively

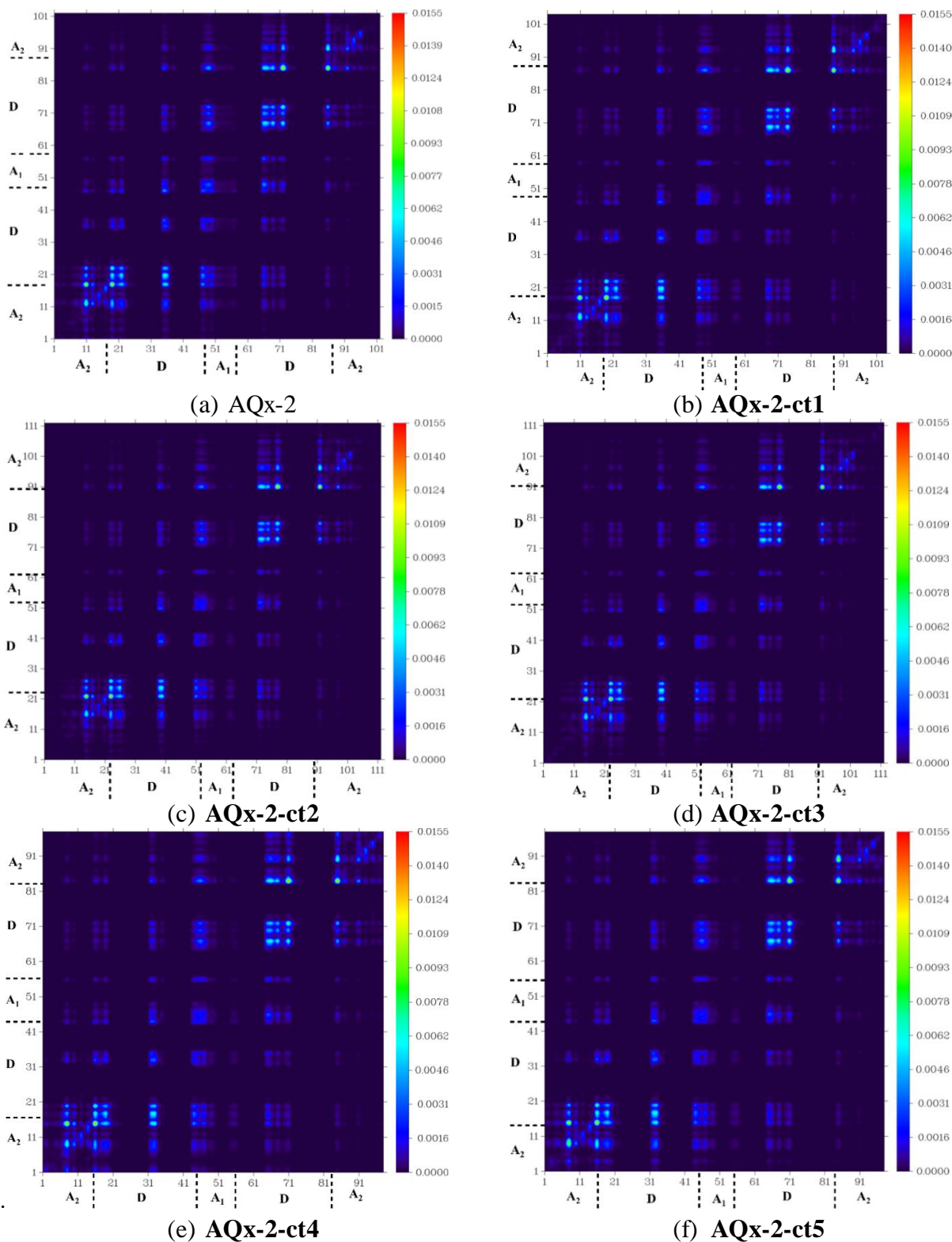


Figure S7. Simulated transition density matrix (TDM) at the CAM-B3LYP/6-31G(d,p) level of theory associated with the $S_0 \rightarrow S_1$ transition of the studied NFAs (AQx-2, AQx-2-ct1, AQx-2-ct2, AQx-2-ct3, AQx-2-ct4, and AQx-2-ct5) in Chloroform solvent (the hydrogen atoms of all molecular systems are

omitted) and the color bars are given on the right

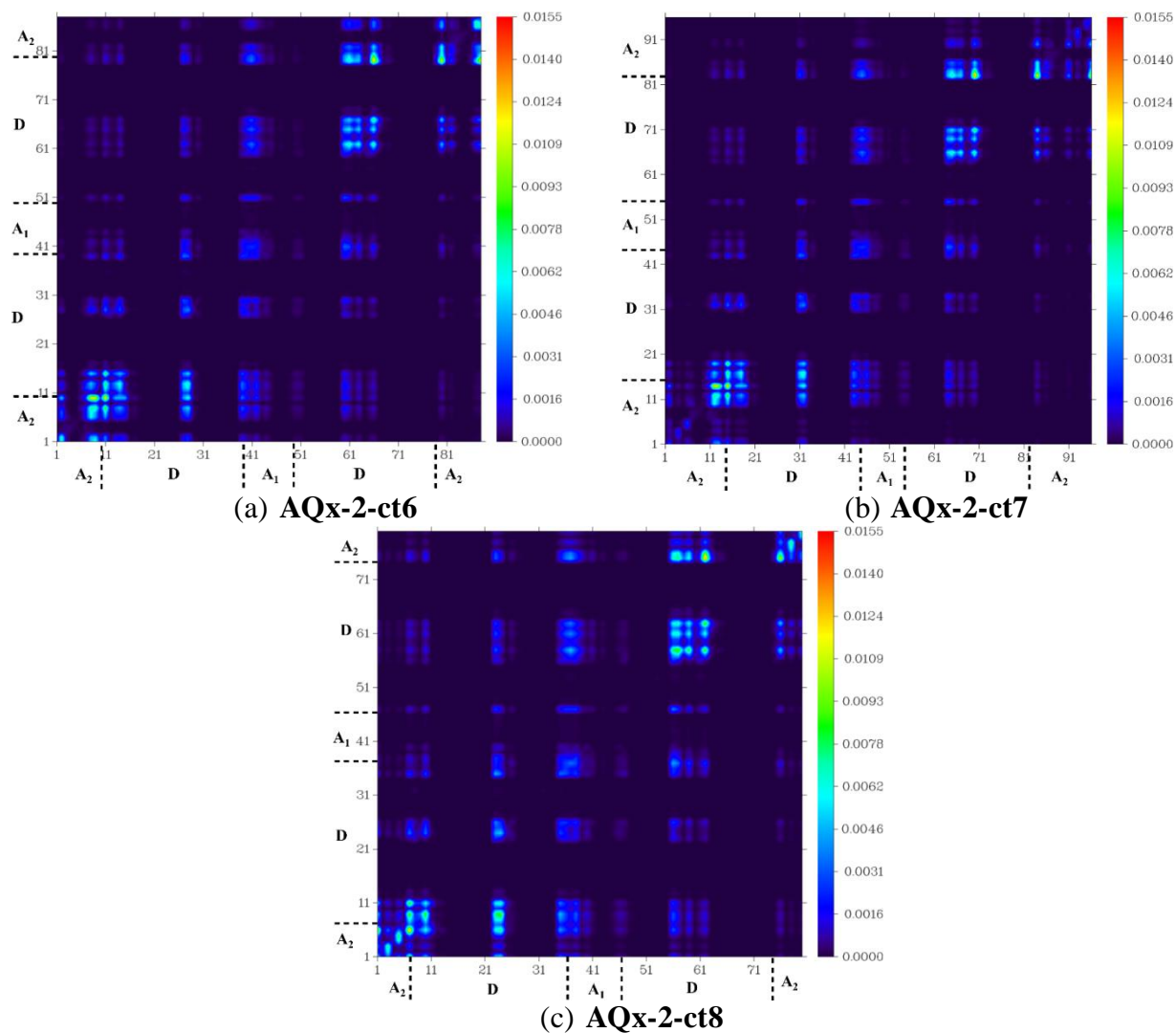


Figure S8. Simulated transition density matrix (TDM) at the CAM-B3LYP/6-31G(d,p) level of theory associated with the $S_0 \rightarrow S_1$ transition of the studied NFAs (AQx-2-ct6, AQx-2-ct7, and AQx-2-ct8) in Chloroform solvent (the hydrogen atoms of all molecular systems are omitted) and the color bars are given on the right

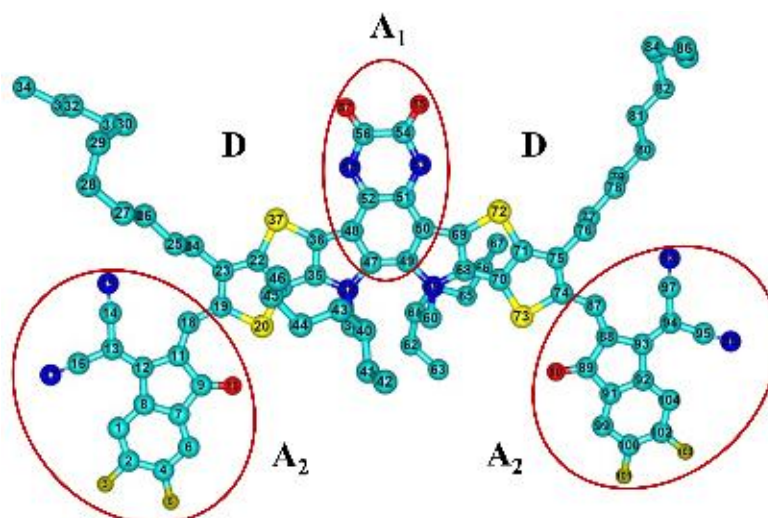
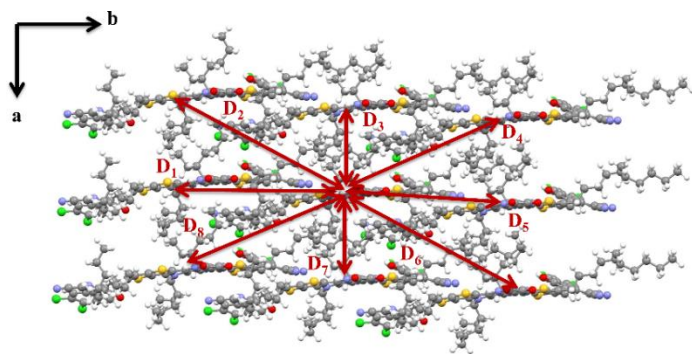
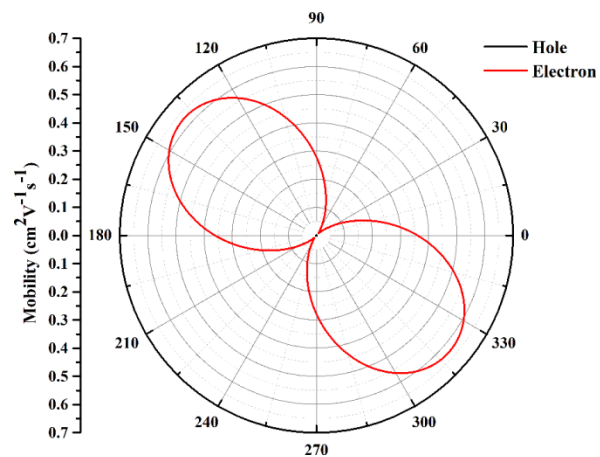


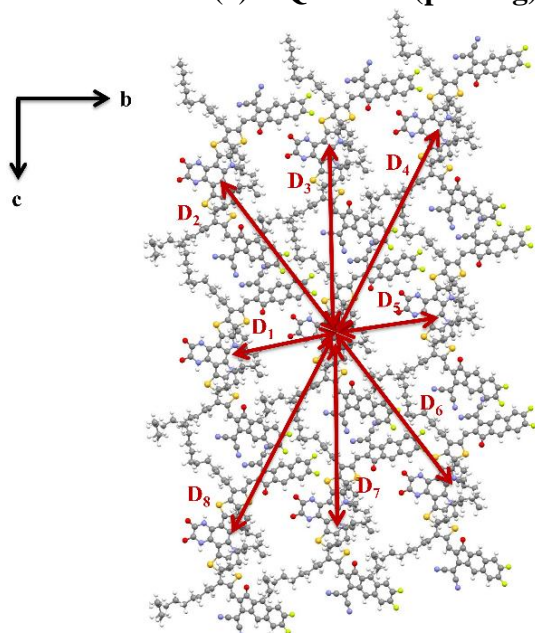
Figure S9. The atom numbering of the designed NFAs (NFA: **AQx-2-c**) corresponding to TDM mapping. The cyan, yellow, blue and greenish yellow represent carbon, sulfur, nitrogen, oxygen and fluorine atoms, respectively.



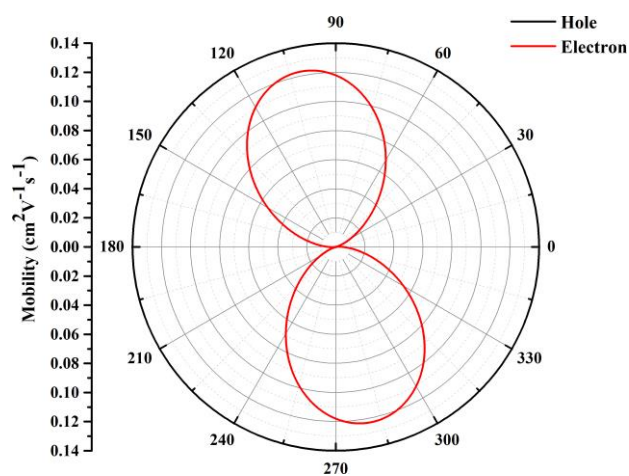
(a) AQx-2-ct1 (packing)



(b) AQx-2-ct1 (mob)

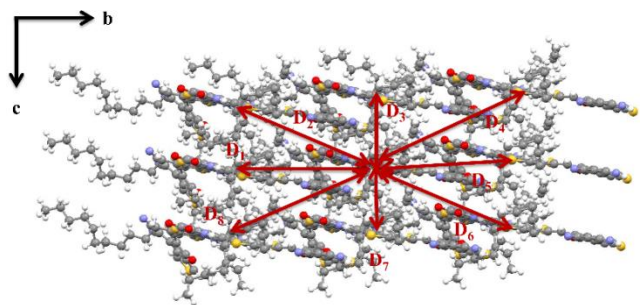


(c) AQx-2-ct2 (packing)

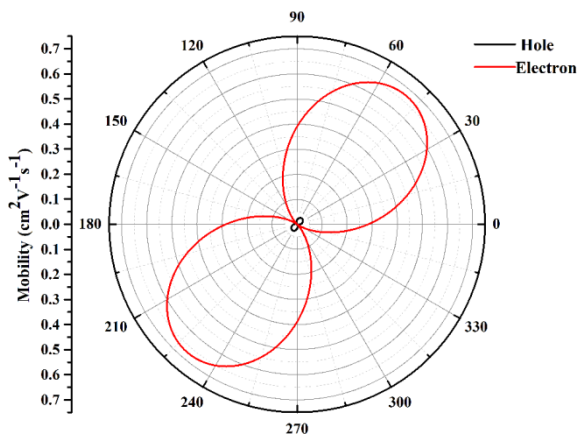


(d) AQx-2-ct2 (mob)

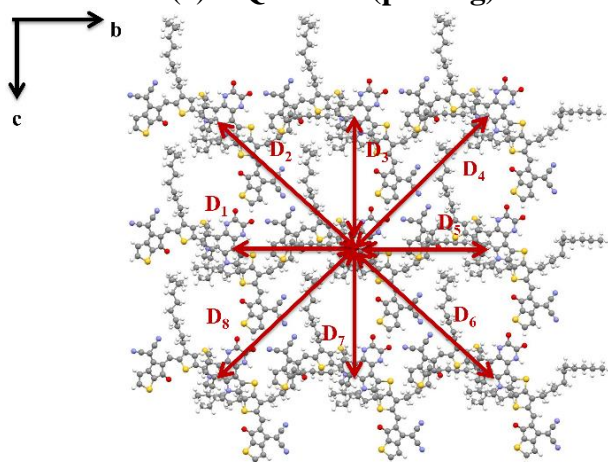
Figure S10. Simulated crystal structures showing different hopping channels and angle resolved anisotropic mobility of the studied NFAs (AQx-2-ct1, AQx-2-ct2)



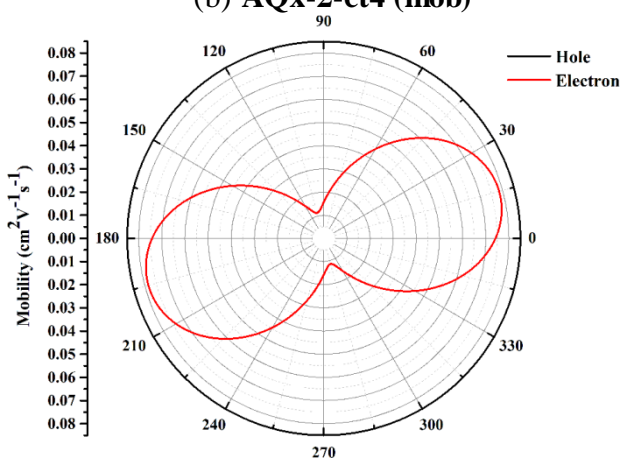
(a) AQx-2-ct4 (packing)



(b) AQx-2-ct4 (mob)

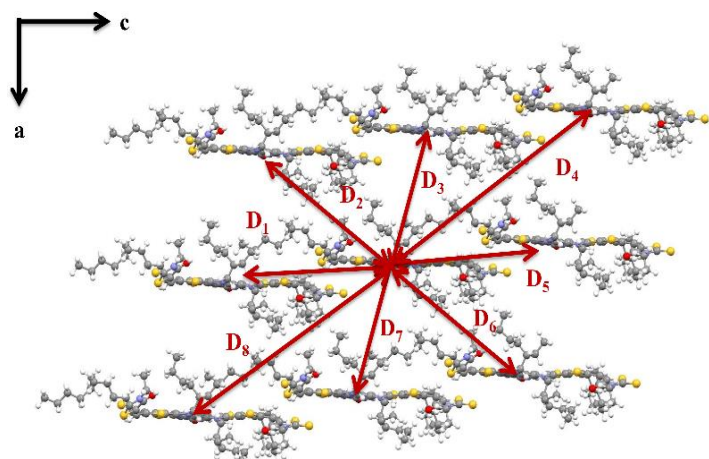


(c) AQx-2-ct5 (packing)

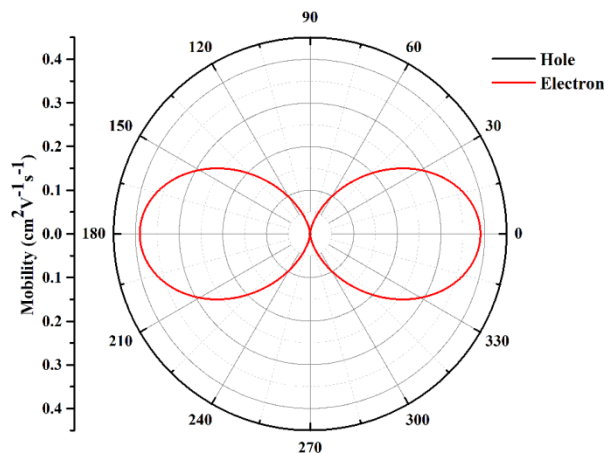


(d) AQx-2-ct5 (mob)

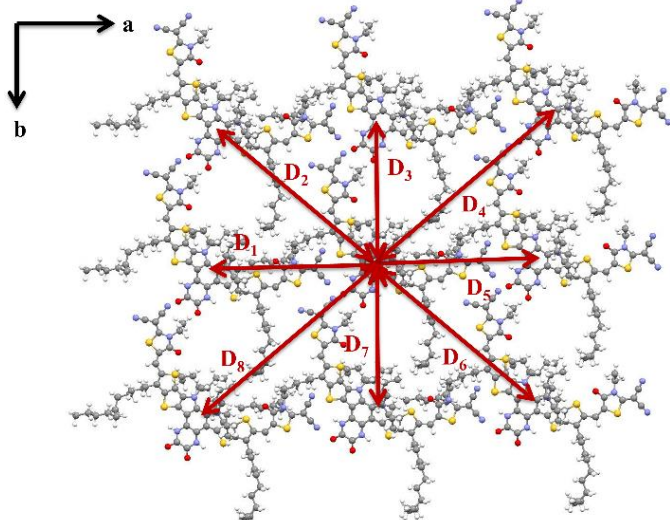
Figure S11. Simulated crystal structures showing different hopping channels and angle resolved anisotropic mobility of the studied NFAs (AQx-2-ct4, and AQx-2-ct5)



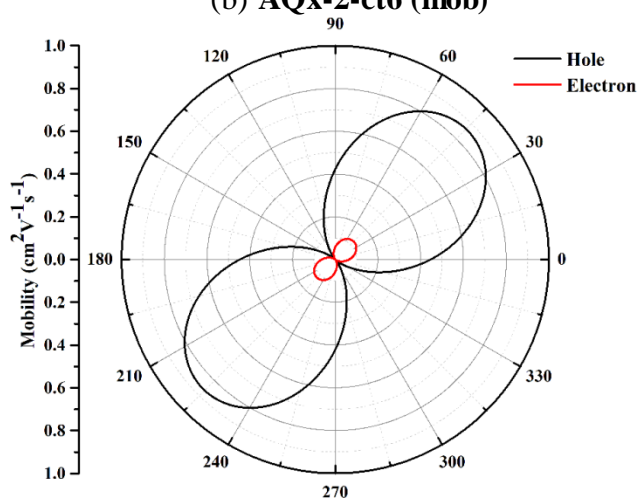
(a) AQx-2-ct6 (packing)



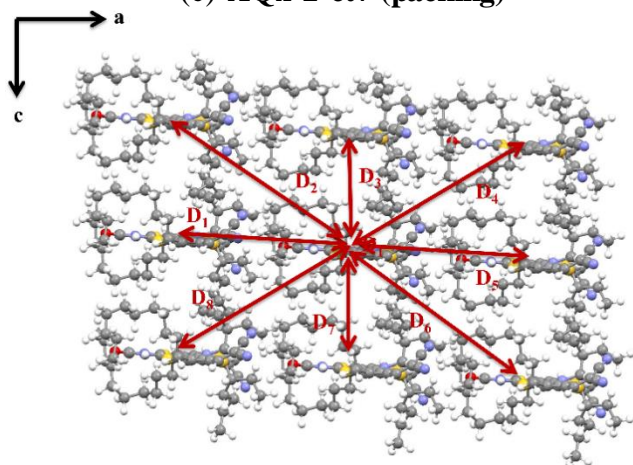
(b) AQx-2-ct6 (mob)



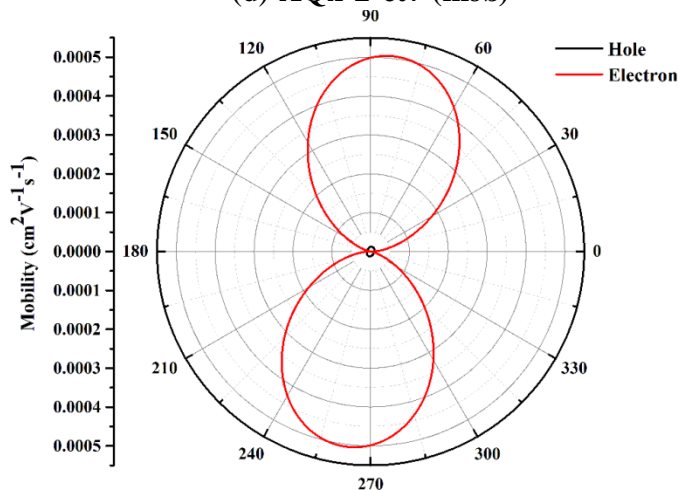
(c) AQx-2-ct7 (packing)



(d) AQx-2-ct7 (mob)



(e) AQx-2-ct8 (packing)



(f) AQx-2-ct8 (mob)

Figure S12. Simulated crystal structures showing different hopping channels and angle resolved anisotropic mobility of the studied NFAs (AQx-2-ct6, AQx-2-ct7, and AQx-2-ct8)

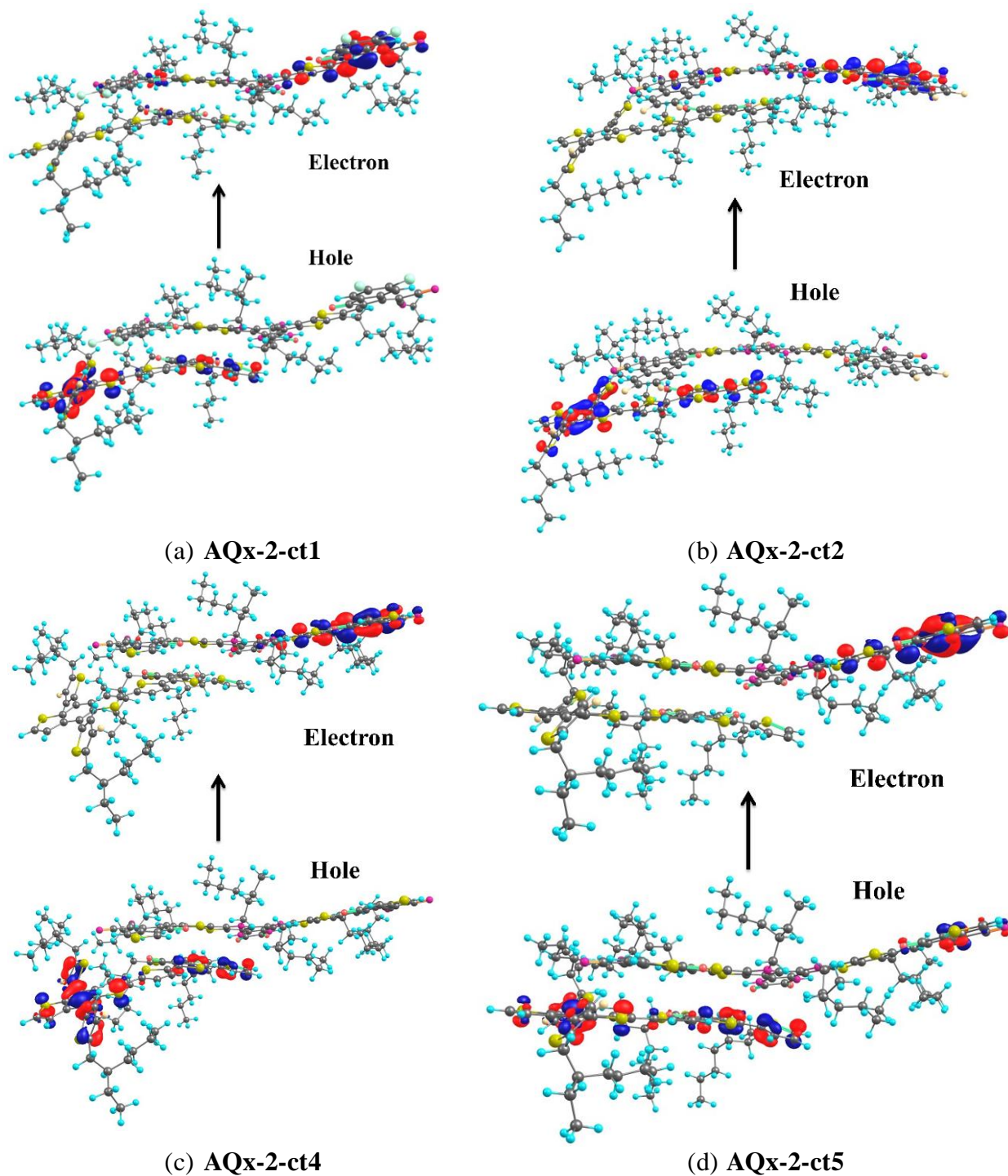


Figure S13. The NTO analysis of the CT excited states of the investigated PM6/NFA (AQx-2-ct1, AQx-2-ct2, AQx-2-ct4, AQx-2-ct5) blends. The blue and red colors represent the positive and negative isosurfaces, respectively

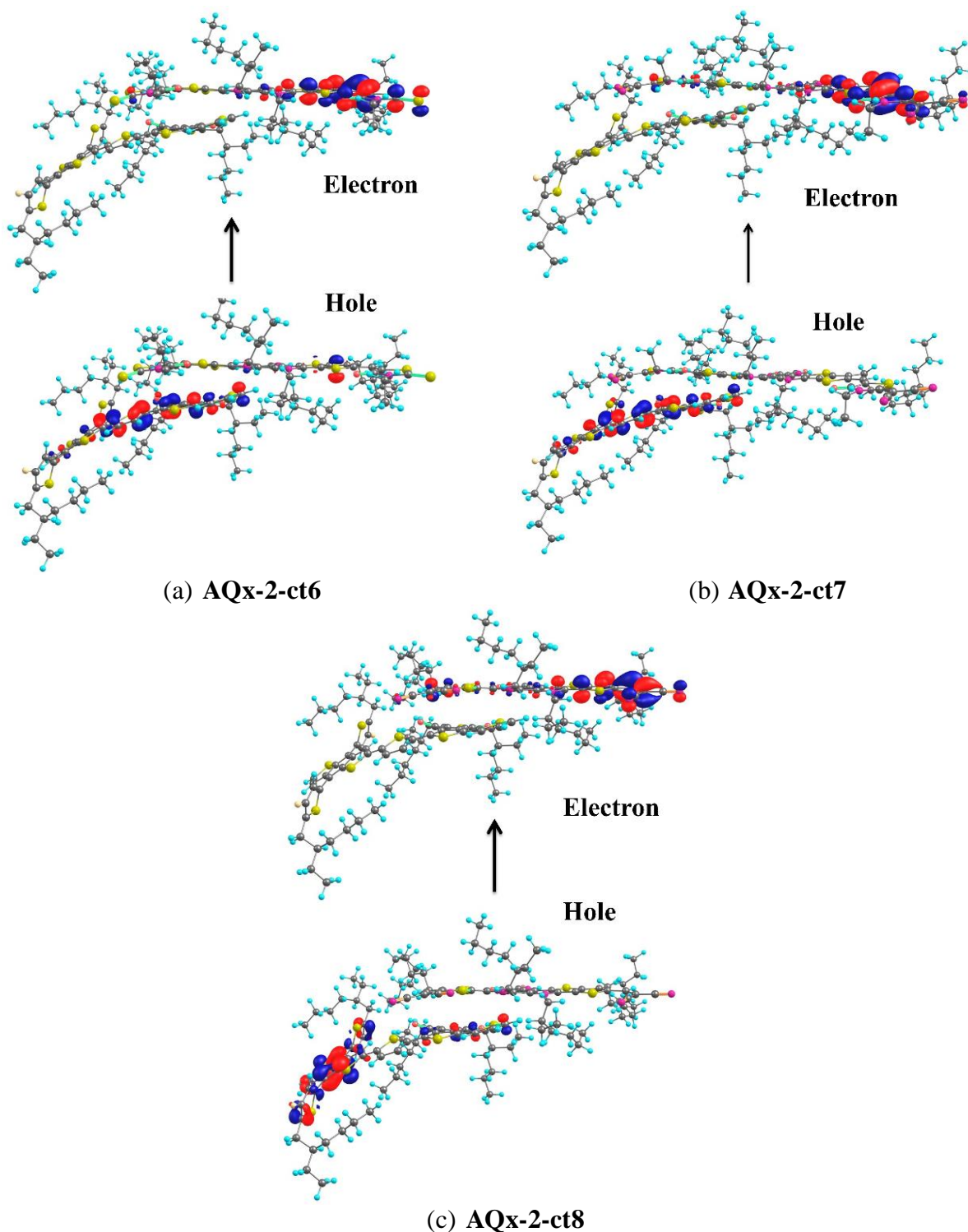


Figure S14. The NTO analysis of the CT excited states of the investigated PM6/NFA (**AQx-2-ct6**, **AQx-2-ct7**, **AQx-2-ct8**) blends. The blue and red colors represent the positive and negative isosurfaces, respectively